UCRL-52806

ENHANCED COUPLING AND DECOUPLING OF UNDERGROUND NUCLEAR EXPLOSIONS

R. W. Terhune
C. M. Snell
H. C. Rodean

September 4, 1979

Work performed under the auspices of the U.S. Department of Energy by the UCLLL under contract number W-7405-ENG-48.

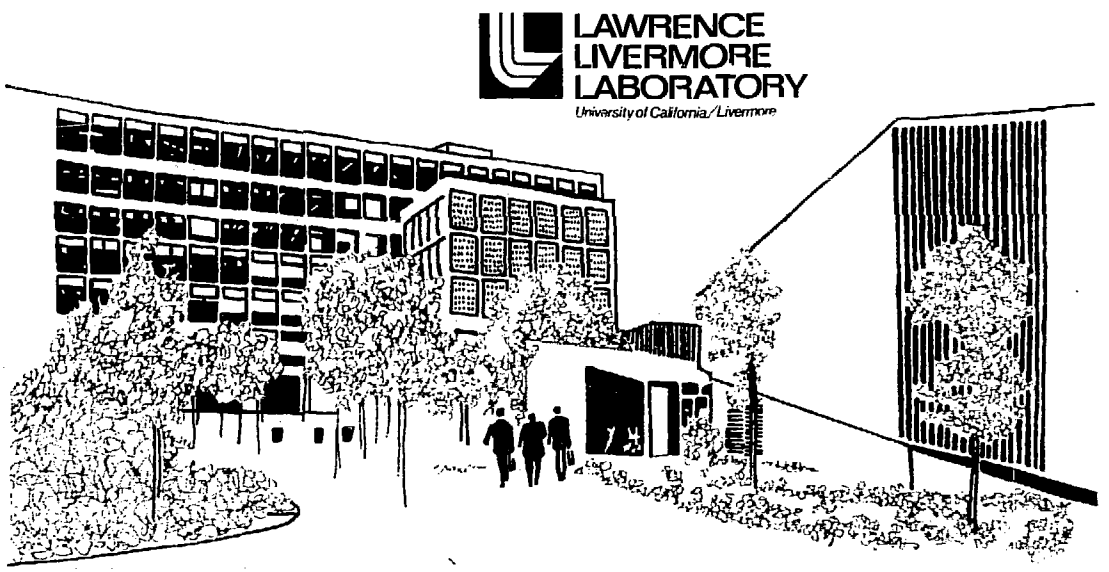

Distribution Category
UC-11

LAWRENCE LIVERMORE LABORATORY
University of California Livermore, California 94550

UCRL-52806

ENHANCED COUPLING AND DECOUPLING OF UNDERGROUND NUCLEAR EXPLOSIONS

R. W. Terhune
C. M. Snell
H. C. Rodean

Manuscript date: September 4, 1979

CONTENTS

Abstract . . . 1
Introduction . . . 1
Previous Work . . . 1
Scope of this Work . . . 2
Elements of this Study . . . 2
The SOC Code . . . 2
Finite-Difference Calculations . . . 2
Material Constitutive Relations . . . 3
Initial Conditions . . . 3
Material Properties . . . 3
Hardhat Granite . . . 3
Gas Equations of State . . . 4
Study Parameters . . . 4
Results . . . 6
Overview . . . 6
Radii of Vaporization . . . 8
Stress Wave Attenuation . . . 12
Elastic Response . . . 15
Discussion with Respect to some NTS Nuclear Events . . . 20
Acknowledgments . . . 22
References . . . 23
Appendix A—Initial Conditions . . . 24
Appendix B—Scaled Results . . . 26

ENHANCED COUPLING AND DECOUPLING OF UNDERGROUND NUCLEAR EXPLOSIONS

ABSTRACT

We studied the seismic coupling efficiency of nuclear explosions in granite by means of computer calculations as a function of scaled explosion source radius. The scaled source radii were varied from 0.1 m/kt$^{1/3}$ (point source) to 20 m/kt$^{1/3}$ (representing a nearly full decoupling cavity). It was found that seismic coupling efficiency is at a maximum when the scaled source radius is approximately 2 m/kt$^{1/3}$. The primary cause of this maximum in seismic wave source strength is the effect of initial source radius on peak particle velocity and pulse duration of the outgoing elastic wave. A secondary cause is that rock vaporization (an energy sink) does not occur for scaled source radii somewhat greater than 1 m/kt$^{1/3}$. Therefore, for scaled source radii greater than 1 m/kt$^{1/3}$, there is additional energy available for seismic wave generations. Available data for some nuclear explosions at the Nevada Test Site do not provide sufficient evidence to either support or negate the enhanced coupling that is indicated by calculations at scaled source radii of 1–2 m/kt$^{1/3}$.

INTRODUCTION

During an AFTAC Seismic Review Panel meeting on 1–2 June 1976, Trulio of Applied Theory, Inc., reported some interesting results from calculations of the seismic coupling of underground nuclear explosions. He performed a series of calculations for explosions in various sizes of spherical cavities in granite. The energy yields of the explosions and the masses of the explosive sources were held constant as the cavity size was varied. Trulio found that, as cavity volume was increased from that for a "tamped" explosion to that for a "decoupled" explosion, the strength of the seismic source function first increased somewhat, then decreased substantially at larger cavity volumes. The maximum seismic signal resulted in a cavity volume somewhat greater than that of the explosive, but much less than that of a full-decoupling cavity. He proposed the following explanation: Seismic coupling reaches maximum efficiency when little or no rock is melted and vaporized, leaving more energy available for mechanical work on the rock. Coupling efficiency declines for source sizes either smaller or larger than this optimum size. Trulio referred to the effect as "enhanced seismic coupling," since an optimum cavity size for seismic energy coupling from a given source is indicated. He suggested that independent calculations be performed to verify this effect. APRA informally asked that the Lawrence Livermore Laboratory make such an investigation. Our independent calculations are discussed in this report.

PREVIOUS WORK

In connection with the Gnome, Salmon, and Sterling explosions, Patterson made a series of calculations of tamped, partially decoupled, and fully decoupled explosions in salt and in granite.[1,2] His calculations did not reveal any enhanced coupling at small cavity radii, but they did indicate decreased coupling with increased ratio of cavity volume to explosion energy. This is because Patterson did not make any calculations for the small cavity volumes at which Trulio noted coupling enhancement.

Patterson's calculations concentrated on near fully decoupled explosions where the scaled cavity or source radius ($R_0/W^{1/3}$) is approximately 30 m/kt$^{1/3}$ for salt and 20 m/kt$^{1/3}$ for granite. The

calculated normalized reduced displacement potential (RDP) for the fully decoupled explosion is on the order of 3.5 m^3/kt. The scaled source radius ($R_0/W^{1/3}$) for the partially decoupled calculations exceeded 13 m/$kt^{1/3}$, which is much larger than the range of scaled source radii for which Trulio noted enhanced seismic coupling.

Patterson compared the effect on the RDP of the detailed explosion phenomena in the cavity with that of assuming the energy is initially distributed uniformly throughout the cavity. For large cavities that would fully decouple an explosion, the detailed cavity phenomena calculations produced the same results at seismic frequencies as calculations based on a uniform initial distribution of energy. However, for partially decoupled explosives, the detailed cavity-phenomena calculations gave RDP values that ranged from one-tenth to three times those of the uniformly distributed energy model, depending on the mass of the nuclear explosive and the scaled source radius. The larger the mass of the device, the greater the difference between the results for the two models.

SCOPE OF THIS WORK

This report presents a series of numerical calculations performed with LLL's underground explosion computer code SOC.[3-6] The calculations are intended to simulate detonations of nuclear explosives in various sizes of cavities in granite approximately 1000 m deep. The primary purpose of the calculations was to determine how the seismic source function (RDP) varies as the initial cavity size is increased from that of an almost point source to that of a fully decoupled cavity. In addition, if Trulio's "enhanced seismic coupling" was observed in our calculations, we would attempt to determine the physical cause of that enhancement.

The source term that we used for the calculations is modeled by a sphere of vaporized iron in which the energy and mass of a nuclear device are uniformly distributed throughout the cavity. This results in a uniform pressure throughout the initial cavity, which initiates the propagation of the shock wave into the surrounding granite medium. This source model is an excellent approximation of a tamped nuclear detonation,[7] but suffers from obvious defects in simulating the source function for partially decoupled explosions. We have ignored the detailed cavity phenomena studied by Patterson (see above) such as shock-wave propagation through the air between the device and the cavity wall, stagnation pressure at the cavity wall, impulse of the device debris impacting on the cavity wall, and subsequent reverberations caused by shock-wave reflections off the cavity wall. The average cavity pressure during the subsequent cavity expansion, however, is believed to be a reasonable approximation to physical reality. Thus, this parametric study should be viewed as an effects study where the energy density, mass density, and source size are varied rather than as a definitive study of partially decoupled detonations.

Part of this study is similar to that done by Trulio in that we used a constant energy source as the cavity size was varied. In addition, we studied the effects of keeping the cavity size constant and varying the energy of the explosion. We correlated the results by applying the principles of similitude as in Hopkinson Blast Scaling.[8]

ELEMENTS OF THIS STUDY

THE SOC CODE

Finite-Difference Calculations

Calculations discussed in this report were made with SOC, a one-dimensional Lagrangian computer code.[3-6] Planar, cylindrical, and spherical geometries are available; we used spherical geometry in this study. SOC models material motion and stress-wave propagation within a grid of discrete material zones. Motion is initiated by an energy source, stress, or velocity condition introduced within the grid, or by an external force applied to the grid. Given the initial stress field, the code solves the equation of motion to obtain the acceleration at each node within the grid. Accelerations acting over a small time interval Δt produce new velocities. The integrated velocities give displacements, which in turn determine new strains. Finally, these strains are used to calculate new stresses for each zone. A general constitutive relation or stress–strain relation describing the behavior

of the material is necessary to calculate these new stresses (see below). Time is then increased by Δt, and the entire process is repeated. The calculation may be carried forward in this manner to examine stress-wave propagation throughout the grid.

Material Constitutive Relations

The physics of material behavior is modeled by the constitutive relations used to calculate the stresses as a function of the strains. Thus, the constitutive models are of crucial importance with respect to the physical validity and accuracy of predictive calculations. The results of this study are constrained by the constitutive models used.

The type of constitutive model used depends in part upon the demands of the problem to be solved. The nuclear-explosion problem involves a broad range of peak stresses, and widely varying regimes of material behavior. A nuclear explosion abruptly releases large amounts of energy within the small volume of the explosive assembly. If the event occurs in a tamped configuration (closely coupled to the surrounding material), a large stress discontinuity forms and moves outward. This shock wave compresses the material, distributing internal and kinetic energy as it propagates. Close to the source, material is vaporized and acts as a fluid. Peak stresses decrease as a result of spherical divergence of the wavefront and energy deposition in the source vicinity. At greater ranges, a region of melted material is formed, and the water component (if any) may be vaporized. This is surrounded by a region of completely crushed and shattered material. Fractured or ductilely distorted material extends outward a considerable distance from the source. Finally, gross inelastic effects cease to occur and the wave propagation becomes almost elastic. This series of events occurs at stresses ranging from about 1000 GPa (vaporized rock) down to 0.01 GPa or less (elastic or quasi-elastic wave propagation).

Initial Conditions

The initial state or starting condition of the computational grid must be specified. All of the calculations discussed here use a grid consisting of two concentric spherical regions: a gas material region representing the energy source, and an initially solid region outside the source. The zone size in the source region is constant, while the zone size in the solid material may be either constant or increasing in geometric progression away from the source. The source region may be modeled as an iron gas sphere (representing the explosive assembly) or as a sphere of uniform rock gas simulating the entire volume of rock vaporized by the detonation. In this study we used an iron gas source. We assumed that the source region has uniform initial material density, energy density, and pressure. The initial density and total energy are chosen to model the mass and energy release of the nuclear explosive. The source radius is based on the size of the initial cavity volume for both "tamped" and "decoupled" explosions.

An initial stress distribution must also be specified for the rock medium outside the cavity. The overburden stress plays a role in halting cavity expansion for deeply buried events; it is particularly important in the case of decoupled explosions because the final cavity pressure is approximately equal to the overburden pressure. Analytic solutions are available for certain cases of interest, such as a spherical cavity in an externally pressurized linear elastic medium.[1] No analytic solution exists for the more general case of a spherical cavity in a gravitationally settling medium. However, numerical techniques may be used to solve this problem. One convenient method developed by Hancock[9] uses a finite-difference scheme to perform mechanical-equilibrium calculations. The method consists of adding a velocity-damping term to the equation of motion in a finite-difference calculation. The equation of motion is then integrated step-by-step with respect to a time-like variable, called "pseudo-time." Proper choice of the damping constant allows rapid convergence to mechanical equilibrium. This mechanical-equilibrium solution capability was added to the SOC code, and was used to establish initial conditions for some of the decoupling calculations.

MATERIAL PROPERTIES

Hardhat Granite

Material properties needed for the calculations include the initial density and elastic constants of the medium, energy content required to liquefy and vaporize, vapor equation of state,[10] and the compressibility and shear strength of solid material. This information is normally obtained from laboratory and field measurements, theoretical and empirical models of rock behavior, studies of

previous tests in similar media, etc. Detailed investigations of the Hardhat and Piledriver events have resulted in the development of a constitutive description intended to model dynamic effects of large-scale nuclear detonations in a dense granitic medium.[11-14] This previously derived description is adopted for the current study. The granite is assumed to be a low-porosity, weak, fully saturated material. The low strength and wet condition are meant to characterize the bulk properties of a jointed and imperfect rock mass. Small uncracked laboratory specimens show higher strengths. Since complete saturation is assumed, the material suffers no irreversible compaction (air void removal) upon loading.

The physical properties adopted for the granite medium are listed in Table 1. These parameters are generally representative of a dense, wet granite formation. The values of some of these parameters are compared in Table 2 with those used by Trulio.

Gas Equations of State

The energy source region and surrounding vaporized rock play a central role in establishing and maintaining the stress field of the explosion. Thus, it is important to have an adequate description of the gas materials. Theoretical models describe the behavior of atomic, molecular, and ionic mixtures within certain regions of energy and density. These models have been incorporated into computer codes which calculate equilibrium state points within the appropriate regions. Butkovich has used the theoretical equation-of-state codes, in conjunction with experimental data, to establish gas equations of state for a variety of natural materials.[10] The results are plotted as pressure vs internal energy for various isochores or curves of constant density. The calculated equations of state include densities from 10^{-5} to 10 Mg/m^3, an interval which encompasses the region of interest for most explosion calculations. The SOC code accepts corresponding tabular equations of state that give pressure as a function of internal energy and density. A two-dimensional interpolation procedure is used to calculate points that lie between two isochoric curves. We used equations of state for iron gas and for a mixture of SiO_2 plus 1% by weight of water vapor to represent the rock.

Most geological formations contain significant amounts of naturally occurring water. Thus, water vaporization effects may influence dynamic interactions close to the detonation. Since water vaporizes at much lower stress levels than does the associated rock material, a means must be provided to take into account the partial-pressure contribution of water vapor. The SOC code utilizes a technique developed by Butkovich.[15]

STUDY PARAMETERS

We made three series of explosion calculations: 11 in the "tamped" (T) series, 15 in the "decoupled" (D) series, and 7 in the "decoupled and relaxed" (DR) series, which are summarized in the tables in Appendices A and B.

In the T series, yield (W) was varied from 1 to 1000 kt, the initial cavity radius (R_0) was varied from 0.1 to 1.20 m, and the initial iron gas density (ρ_0) was varied from 1.5 to 3.23 Mg/m^3.

In the D series, W was constant at 1 kt except for two calculations with W = 1000 kt, where R_0 was varied from 1.2 to 15 m, and ρ_0 was varied from 4.18×10^{-4} to 0.817 Mg/m^3.

In the DR series, W was 1 kt in all cases; R_0 was varied from 2.5 to 23.62 m, and ρ_0 was varied from 2.47×10^{-5} to 9.04×10^{-2} Mg/m^3.

The principal difference between the D and DR series was in the initial rock stress distribution surrounding the cavity. A uniform hydrostatic pressure throughout the granite of 26 MPa was assumed in both the T and D series. In the DR series, the preexplosion stresses in the rock surrounding the cavity were relaxed to an equilibrium state corresponding to zero cavity pressure and an overburden pressure of 26 MPa, except in DR6 and DR7 where an overburden pressure of 18.1 MPa was used.

Our reference "tamped" explosive was assumed to have a mass of 5.91 Mg, an equivalent spherical radius of 0.98 m, and a corresponding density of 1.5 Mg/m^3. Unlike conventional explosives, the energy release from nuclear explosives is almost independent of the mass and volume of the explosive assembly. Two nuclear explosives can have approximately the same mass and volume but have yields that differ by an order of magnitude or more. Both explosives could be emplaced in a "tamped" configuration, but would have different seismic source characteristics. Similarly, both explosives could be emplaced in a "decoupling" cavity, but their seismic source characteristics would differ. Therefore, we summarized our results

TABLE 1. Material properties for Hardhat granite.

1 MATERIAL 51 CONSTANTS HARDHAT GRANITE (FROM RT0713SCN)

IN GRAMS/CC DENSITY	SHEAR MOD. OR POISSONS RATIO	BRITTLE-DUCT. TRANSITION	MAXWELL RELAX TIME	SHEAR STRAIN FOR FAILURE	SHOCK WITH IN SOLID	
2.670000E+00	2.800000E-01	3.000000E-02*	3.997380E+01*	1.000000E-02	-2.000000E-01	
WATER FRACTION	WATER VAPOR VOL. STRAIN	MU AT 1.2 MAT VAP. PRES.	ENERGY TO MELT	ENERGY TO VAPORIZE	GAS MODE INDICATOR	NON-SOLID LIN. Q FACTOR
1.000000E-02	1.500000E-01	7.279016E-02	1.315810E-01	4.711644E-01	-1.000000E+02	2.000000E-01
MU = 1	A-1 CONSTANT	A-2 CONSTANT	A-3 CONSTANT	CALCULATED: MU-2	BULK MODULUS	SOUND SPEED
0.	1.000000E+00*	0.	0.	0.	4.684351E-01	5.441153E-01

MAX. ALLOWED SHEAR MOD.	HIGH-PRESSURE (2ND)B-D TRANS	HIGH-PRESSURE MAXWL RLX.	DEVIATOR-Q MULTIPLIER	SLOPE A1 (PUTFAH-PETRA)	ULTIM. STRENGTH (PUTT-PET)	P-HAT-PRESSURE (PUT-PET)	COHESION A0 (PUT-PET)
0.	0.	0.	0.	0.	0.	0.	0.

A-EXPONEN(PUT-PET)	B-EXPONEN	INTERCEPT(PUT-PET)	TAU(PUT-PET)	POROUS DAMPING	BDP14	BDP15
0.	0.	0.	0.	0.	0.	

* - INPUT WAS EITHER CHANGED OR *THE DEFAULT VALUE USED*

PRESSURE-VOLUME-VOL. STRAIN TABLES

LOADING TABLE

P	V	MU	DP/DMU
0.	3.743532E-01	0.	4.684435E-01
1.000000E-03	3.737834E-01	2.134777E-03	4.684435E-01
2.000000E-03	3.732947E-01	4.249949E-03	4.728175E-01
3.000000E-03	3.721837E-01	6.300153E-03	4.876475E-01
5.000000E-03	3.707206E-01	1.028221E-02	5.022448E-01
7.000000E-03	3.693365E-01	1.440708E-02	5.279008E-01
1.000000E-02	3.673306E-01	1.960597E-02	5.419955E-01
1.500000E-02	3.647226E-01	2.688555E-02	6.864352E-01
2.000000E-02	3.624721E-01	3.327111E-02	7.830125E-01
3.000000E-02	3.583151E-01	4.525864E-02	8.342116E-01*
4.000000E-02	3.542001E-01	5.740211E-02	8.234844E-01*
6.000000E-02	3.459005E-01	8.559951E-02	7.092853E-01*
1.000000E-01	3.266001E-01	1.467601E-01	6.540171E-01*
2.000000E-01	2.829002E-01	3.239028E-01	5.645201E-01*
3.000000E-01	2.448001E-01	5.299501E-01	4.853231E-01
4.000000E-01	2.272001E-01	6.484601E-01	8.437591E-01
5.000000E-01	2.118001E-01	7.180361E-01	1.437441E+00
7.000000E-01	2.079001E-01	8.015001E-01	2.396241E+00
1.000000E+00	1.995001E-01	8.773531E-01	3.955041E+00
1.500000E+00	1.912002E-01	9.588491E-01	6.135271E+00
2.000000E+00	1.856001E-01	1.017951E+00	8.459781E+00
1.982001E+01	1.000001E-01	2.743532E+00	1.031631E+01

UNLOADING TABLE

P	V	MU	DP/DMU
0.	3.743532E-01	0.	4.684435E-01
1.000000E-03	3.737834E-01	2.134777E-03	4.684435E-01
2.000000E-03	3.732947E-01	4.249949E-03	4.728175E-01
3.000000E-03	3.721837E-01	6.300153E-03	4.876475E-01
5.000000E-03	3.707206E-01	1.028221E-02	5.022448E-01
7.000000E-03	3.693365E-01	1.440708E-02	5.279008E-01
1.000000E-02	3.673306E-01	1.960597E-02	5.419955E-01
1.500000E-02	3.647226E-01	2.688555E-02	6.864352E-01
2.000000E-02	3.624721E-01	3.327111E-02	7.830125E-01
3.000000E-02	3.583151E-01	4.525864E-02	8.342911E-01*
4.000000E-02	3.542001E-01	5.740211E-02	8.234844E-01*
6.000000E-02	3.459005E-01	8.559951E-02	7.092853E-01*
1.000000E-01	3.266001E-01	1.467601E-01	6.540171E-01*
2.000000E-01	2.829002E-01	3.239028E-01	5.645201E-01*
3.000000E-01	2.448001E-01	5.299501E-01	4.853231E-01
4.000000E-01	2.272001E-01	6.484601E-01	8.437591E-01
5.000000E-01	2.118001E-01	7.180361E-01	1.437441E+00
7.000000E-01	2.079001E-01	8.015001E-01	2.396241E+00
1.000000E+00	1.995001E-01	8.773531E-01	3.955041E+00
1.500000E+00	1.912002E-01	9.588491E-01	6.135271E+00
2.000000E+00	1.856001E-01	1.017951E+00	8.459781E+00
1.982001E+01	1.000001E-01	2.743532E+00	1.031631E+01

* - DENOTES PHASE CHANGE

SHEAR STRENGTH -- PRESSURE TABLES

LOADING TABLE

E	P	DE/DP	PBAR
0.	-1.000000E+00	0.	-1.000000E+00
0.	-5.000001E-05	0.	-5.000001E-05
5.000000E-04	5.000000E-04	9.090911E-01	9.666700E-04
8.000000E-04	1.000000E-03	6.000000E-01	1.266700E-03
1.130000E-03	2.000000E-03	3.300000E-01	2.036700E-03
1.460000E-03	3.000000E-03	3.300000E-01	3.436700E-03
1.950000E-03	5.000000E-03	2.450000E-01	5.458000E-03
2.245000E-03	7.000000E-03	1.475000E-01	7.748300E-03
2.550000E-03	1.000000E-02	1.016670E-01	1.068500E-02
2.985000E-03	2.000000E-02	4.350000E-02	2.069950E-02
3.190000E-03	3.000000E-02	2.050000E-02	3.106300E-02
3.280000E-03	4.000000E-02	9.000000E-03	4.109300E-02
3.300000E-03	5.000000E-02	2.000000E-03	5.110000E-02
3.300000E-03	1.000000E+00	0.	1.001110E+00

UNLOADING TABLE

E	P	DE/DP	PBAR
0.	-1.000000E+00	0.	-1.000000E+00
0.	0.	0.	0
5.800000E-04	1.000000E-03	5.800000E-01	1.193300E-03
9.700000E-04	2.000000E-03	3.900000E-01	2.323300E-03
1.250000E-03	3.000000E-03	2.800000E-01	3.416700E-03
1.655000E-03	5.000000E-03	2.025000E-01	5.551700E-03
1.940000E-03	7.000000E-03	1.625000E-01	7.666000E-03
2.350000E-03	1.000000E-02	1.233333E-01	1.078300E-02
3.300000E-03	5.000000E-02	2.375000E-02	5.111000E-02
3.300000E-03	1.000000E+00	0.	1.001110E+00

TABLE 2. Material properties assumed for hardhat granite (RT0713SCN) compared with those used by Trulio.

Property	This study	Trulio study
Initial density at zero pressure (ρ_0), g/cm^3	2.67	2.7
Elastic Poisson's ratio (ν)	0.28	0.28
Total porosity (ψ)	0.0267	0
Saturation (S)	1.0 or 100%	0
Grain density (ρ_g), g/cm^3	2.7158	2.7
Water content by weight (Z)	0.01	0
Peak pressure to vaporize water, GPa	10.18	–
Energy to liquefy granite, Mb–cm^3/g	0.0493	0.035
Energy to vaporize granite, Mb–cm^3/g	0.1767	0.035
Initial zero-pressure bulk modulus, GPa	46.84	57.6
Initial zero-pressure sound speed, cm/μs	0.544	0.6
Intact tensile strength, GPa	0.005	?
Intact unconfined strength, GPa	0.01	?

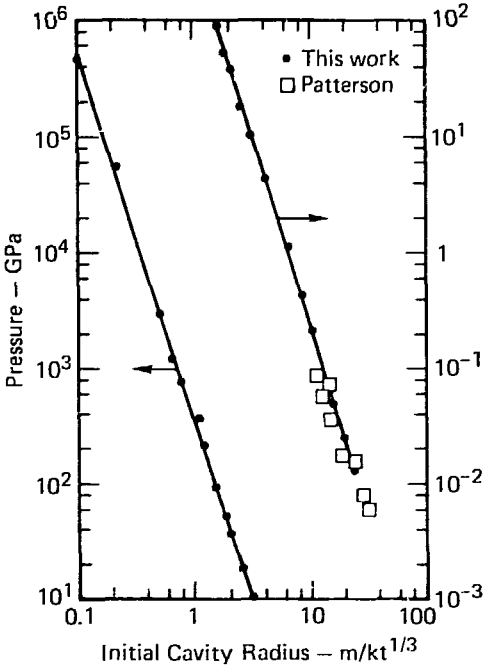

FIG. 1. Initial cavity pressure vs scaled cavity radius.

in terms of parameters scaled to the energy release with length and time referenced to the cube root of the explosion yield. Our assumed uniform overburden pressure conditions and zero gravity condition are compatible with such scaling. As shown below, there are no clear-cut distinctions between "tamped" and "decoupled" nuclear explosions. Rather, these are variations within and a transition between these two classes of explosions, which are a function of scaled source radius.

In Fig. 1, we show the initial iron gas or cavity pressure as a function of scaled initial cavity radius for all our calculations. The initial cavity pressures for Patterson's[1,2] calculations are also given. It is shown that Patterson considered cases that are near or at the fully decoupled condition (scaled cavity radii of approximately 10 to 30 m/kt$^{1/3}$). By full decoupling, we mean that the explosion does not cause any inelastic behavior of the rock. In this work, we have extended the work of Patterson to a near-point source (scaled cavity radius of 0.1 m/kt$^{1/3}$).

Appendix A gives the initial conditions for each calculation.

RESULTS

OVERVIEW

Appendix B gives a summary of the scaled results from each calculation of the parameter study.

The effect, as reported by Trulio, of enhanced seismic coupling for partially decoupled sources was confirmed in this parametric study. Figure 2 is a plot of the final reduced displacement potential (RDP) in the elastic region as a function of the initial cavity radius scaled to the cube root of the energy of the device within the cavity. The initial scaled source radii are an inverse function of the initial energy density and vary from 0.1 m/kt$^{1/3}$ to

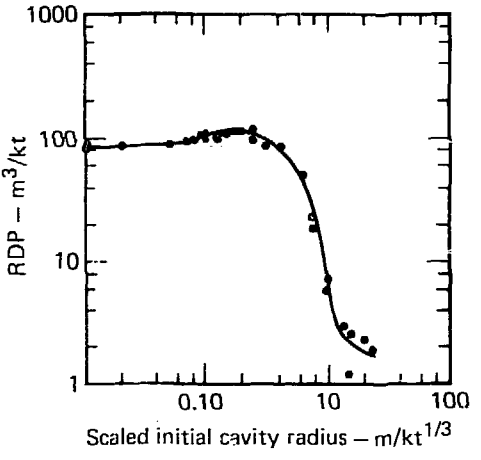

FIG. 2. Final RDP vs scaled initial source size.

about 20 $m/kt^{1/3}$, which represents a variation between almost a point source tamped to an almost fully decoupled cavity. The calculation with an initial scaled source radius of 1.8 $m/kt^{1/3}$ gave the maximum RDP, which was 47% greater than the RDP obtained for a near-point source. The RDP for an almost fully decoupled cavity is about 2 to 3% of that obtained for a point source and is in excellent agreement with the results of Patterson.

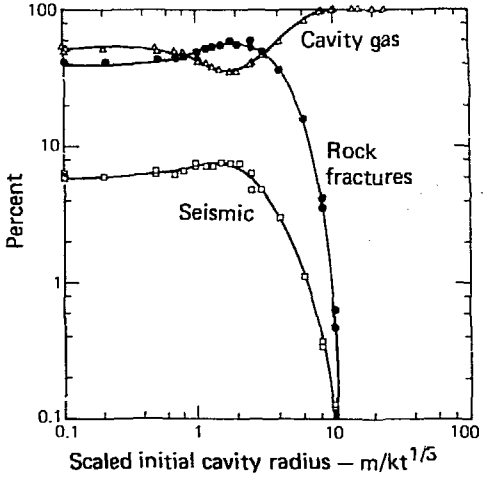

FIG. 3. Final energy balance vs scaled initial source size.

The same characteristics of the RDP curve in Fig. 2 are evident in the seismic energy balance curve shown in Fig. 3. Figure 3 is a plot of the energy balance in three well-defined regions at the end of the calculations as a function of the scaled source radii. These regions are the internal energy in the cavity region, the internal energy dissipated in the fractured rock, and the internal plus kinetic energy in the elastic region, which has been designated the seismic energy. At a scaled source radius in the neighborhood of 2.0 $m/kt^{1/3}$, both the energy trapped in the fractured rock and the seismic energy are near maximum, while the residual internal energy in the cavity is at a minimum. The energy in the cavity includes the potential energy of cavity gas due to its pressure, the energy required to vaporize and melt the rock, and the energy required to vaporize the *in situ* water. Vaporization of the rock occurs only for scaled source radii less than 1.1 $m/kt^{1/3}$, with a significant reduction of the mass of rock vaporized compared to that for a point source for scaled source radii between 0.7 to 1.1 $m/kt^{1/3}$. Melting of the rock occurs only for scaled source radii less than 2.0 $m/kt^{1/3}$ and water vaporization occurs for scaled source radii up to 3.0 $m/kt^{1/3}$. Thus the internal energy of the cavity reflects these various energy-loss mechanisms as the scaled source size is varied from a point source to larger radii. The coincidence of the scaled source size for which melting ceases and the maximum at which the RDP occurs, suggested to Trulio that the enchanced coupling is due entirely to the additional energy that is not being utilized to vaporize and melt the rock. The parametric study reported here shows that another phenomenon in addition to the energy disposition is involved in the enhanced coupling effect. This will be discussed later.

Figure 4 shows the scaled radii at which some of the major changes in the state of the rock occurred as a function of scaled source radii. The curves shown in Fig. 4 are the radius of rock vaporization, the radius of *in situ* water vaporization, the final cavity radius, and the elastic radius or the limiting distance to where fracture occurred. The straight line at 45° represents the initial source size. The amount of rock vaporized is essentially constant for scaled source radii from 0.1 $m/kt^{1/3}$ (point source) to 0.8 $m/kt^{1/3}$ and is much larger than the amount of iron gas over this range. Beyond a source radius of 0.8 $m/kt^{1/3}$ the amount of rock vaporized decreases rapidly and the iron gas becomes the dominant cavity gas.

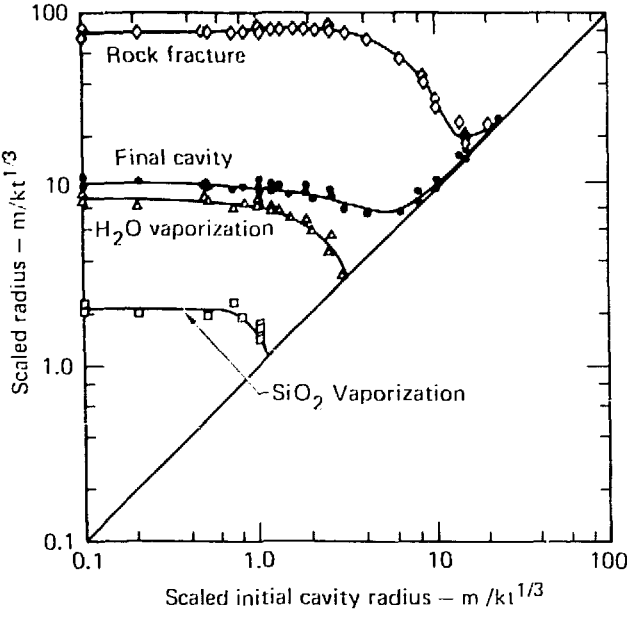

FIG. 4. Radii of major states of rock vs scaled initial source size.

The scaled distance to which the *in situ* water is vaporized is essentially constant for scaled source radii between 0.1 to 1.0 m/kt$^{1/3}$, then decreases to zero at a scaled source radius of 3.0 m/kt$^{1/3}$. The effect of the water vaporization was deemed negligible on the enhanced seismic coupling.

The elastic radius is shown to be essentially constant over the range of scaled source radii between 0.1 and 3.0 m/kt$^{1/3}$. The elastic radius varies between 80–85 m/kt$^{1/3}$ with a broad peak at about a scaled source size of 2.0 m/kt$^{1/3}$, in agreement with the RDP curve (Fig. 2). Beyond a scaled source radius of 10 m/kt$^{1/3}$, very little of the rock is fractured and the stress wave is essentially elastic beyond the source cavity boundary.

Figure 5 shows a comparison of the final cavity pressure with the initial cavity pressure as a function of scaled cavity radii. As the initial source cavity is increased to larger values from a point source, the final cavity pressure also increases until a peak is reached at $R_0 = 6.0$ m/kt$^{1/3}$. These high cavity pressures have interesting implications for the containment of the radioactive gas for partially decoupled events.[16]

RADII OF VAPORIZATION

The plots of reduced displacement potential and other physical quantities show an apparent discontinuity near a scaled source radius of 0.98 m/kt$^{1/3}$. The RDP, for example, increases by about 11% between source radii of 0.686 and 0.98 m/kt$^{1/3}$ (Fig. 2). It then increases more slowly and continuously at radii just above 0.98 m kt$^{1/3}$. This abrupt change in behavior may be explained in terms of rock vaporization by the nuclear event. Those detonations with initial source radii less than about 0.98 m/kt$^{1/3}$ vaporize very large masses of surrounding rock. Events with initial radii near 0.98 m/kt$^{1/3}$ fully vaporize a significantly smaller amount of rock, corresponding to only a few zones in the finite-difference grid. No vaporization occurs for source radii greater than 1.1 to 1.2 m/kt$^{1/3}$ in these calculations; of course, some heating, liquefaction, and water vaporization may still take place for larger-radii sources. This transition from vaporizing to non-vaporizing behavior occurs rather abruptly because the initial pressure and energy density drop off rapidly with increasing

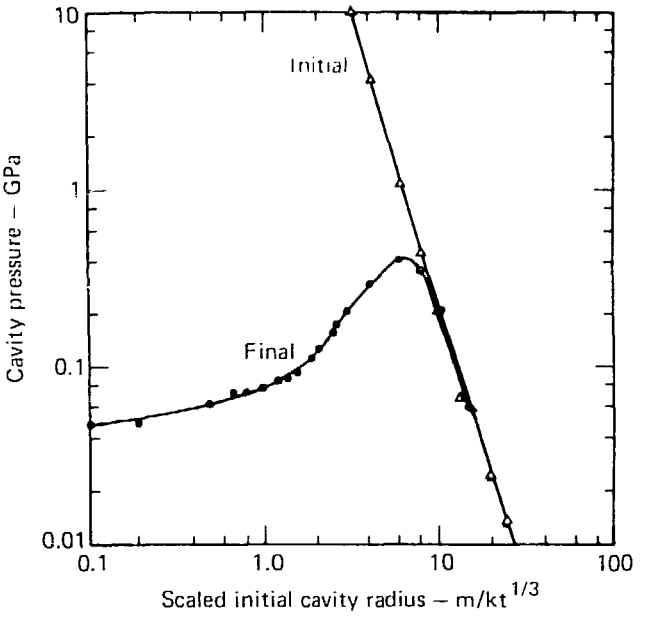

FIG. 5. Initial and final cavity pressure vs scaled initial source size.

source radii. The transition radius at which rock vaporization ceases to play a crucial role lies very close to 0.98 $m/kt^{1/3}$.

In order to investigate the relationship between rock vaporization and energy coupling, we have closely examined three typical 1 kt calculations, i.e., events T6, T9, and T10, for source radii R_0 of 0.686 m, 0.98 m, and 1.2 m. The corresponding initial source pressures were 106 GPa (extensive rock vaporization), 38 GPa (small amount of rock vaporization), and 20 GPa (no rock vaporization). The initial source densities were 1.5 g/cm^3 in all cases. The zoning varied somewhat among the three problems, but results were similar for other comparable calculations and were not critically influenced by zone size. Figure 6 shows the iron gas source mass, the mass of rock vaporized, and the mass of material with the water component vaporized for the three events. Note that the mass of rock vaporized is large for the 0.686 m event, but is much smaller and hardly greater than the iron gas source mass for the 0.98 m event. No rock was vaporized in the 1.2 m event.

The influence of energy-source pressure and shock-loading behavior of the surrounding rock on energy coupling has previously been studied.[17] The peak pressure and the response of material to the outward-going shock wave govern the amount of energy lost to shock heating and thereby the close-range coupling efficiency. Figure 7 schematically shows the response of a dense solid material of initial specific volume V_0 to shocks of varying amplitude. For low-pressure loading, the material loads along a Rayleigh line and unloads close to the initial Hugoniot line (little shock-heating effect). The PdV expansion work available from the material is approximated by the area under the Hugoniot line, while the waste heat or energy loss that does no work on the surroundings is given by the area between the Rayleigh line and the Hugoniot line. The waste heat is seen to be relatively small in this case. For high-pressure loading, the material loads along a much steeper Rayleigh line. The increased internal energy is sufficient to cause vaporization. The hot vapor material unloads to expanded (larger) specific volumes at low pressures. In spite of this increased expansion, an enormous amount of energy is lost as excess waste heat. Thus, much of the energy is retained as internal heat and energy coupling to greater ranges is actually *less* efficient for the high-pressure loading case (vaporized material). Those

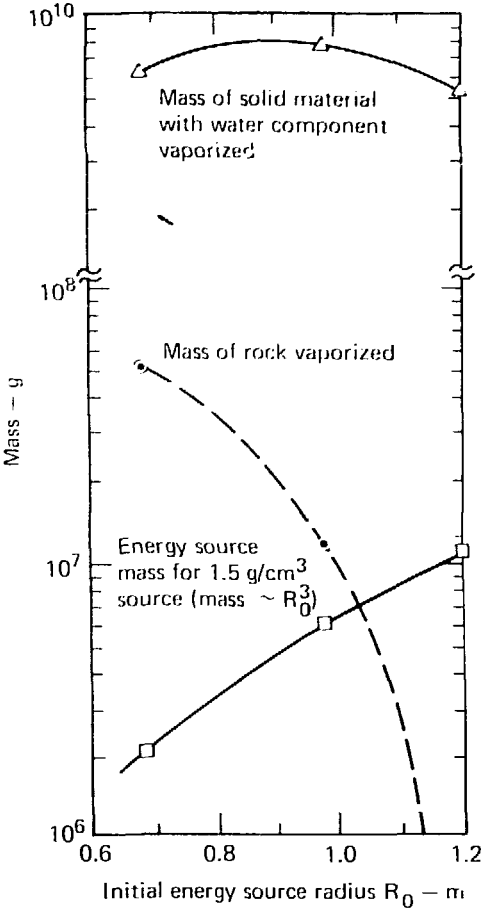

FIG. 6. Vapor material masses for 1 kt SOC calculations, source radii R_0 = 0.686 to 1.2 m/kt$^{1/3}$.

events that vaporize a significant amount of rock ($R_0 < 0.98$ m/kt$^{1/3}$) will suffer large shock-heating energy losses of this type, resulting in less-efficient coupling.

The approximate late-time volumetric expansion paths for the iron gas sources in the three sample problems are shown in Fig. 8. The source regions unload to a pressure of about 0.1 GPa at a time of 10 ms, the cutoff time for this plot. The small-radius problem R_0 = 0.686 m has the highest expansion path and the greatest final volume expansion, because it started at the highest initial pressure and internal energy density. However, the final iron gas radius R = 7.107 m is smallest in this case because of the smaller initial radius. The expanding iron gas initiates the shock wave which first vaporize rock material beyond the initial contact interface. The unloading paths of the rock vapor are of direct interest, since they are indicative of the local energy deposition. Figure 9 presents late-time expansion behavior of the rock gas in problems R_0 = 0.686 m and R_0 = 0.98 m. These are average paths on several typical zones. The rock material in problem R_0 = 0.98 m is shocked only slightly above the vaporization point. Thus its energy density is lowest and the unload path is also lowest (smallest volumetric expansion at a given pressure). The vapor zone farthest from the source in problem R_0 = 0.686 m experiences a similar peak pressure and follows an almost identical low unloading path. However, the zones closer to the source for R_0 = 0.686 m experience intense shock loading, receive much greater internal energies, and follow higher unloading paths. The intermediate unloading path shown in Fig. 9 represents a zone about halfway through the rock gas region, while the highest path is for the vaporized zone adjacent to the iron gas source.

The effect of vaporization on energy coupling may be examined by plotting the energy content in each material as a function of time. Figures 10 and 11 present the calculated energies in the iron-gas source region, rock-vapor region, vaporized-water region, and solid granite region as functions of time. These energies are divided into kinetic and internal components, except in the case of the iron gas source, which possesses negligible kinetic energy.

Figure 10 demonstrates that the energy retained in the iron gas declines steadily with time, as the source expands and couples to the environment. The relative amount of energy in the source at a given time is greatest for the 1.2 m source (largest, most massive source region), and is least for the small 0.686 m source.

The energy contained in rock vapor presents a different picture (Fig. 10). Both the internal and kinetic energies are greatest for the 0.686 m event, and decrease by a factor of four to six for the 0.98 m event (which vaporized only a small amount of rock). The 1.2 m event did not vaporize any rock material. Note that the internal energy in rock vapor is a very significant fraction of the total energy for the 0.686 m source. This fact is closely related to the waste-heat energy loss and the less-efficient coupling for the 0.686 m event. Energy deposition in rock vapor is small or nonexistent for the other two cases.

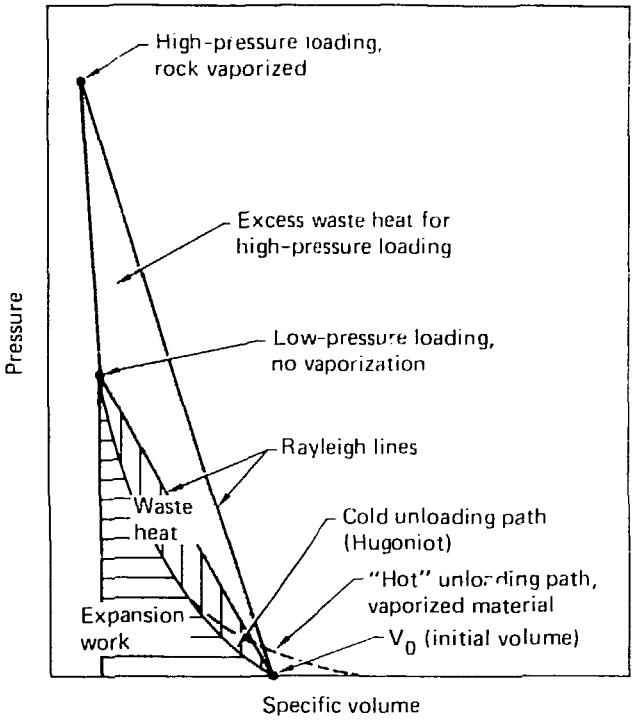

FIG. 7. Shock loading and vaporization of rock.[17]

The internal energy in the vaporized water region shows a similar trend (Fig. 10): it is greatest for the 0.686 m event (strong shock at close ranges), slightly less for the 0.98 m event, and much less for the 1.2 m event. The kinetic energy in the vaporized-water region displays somewhat less consistent behavior, with the highest value (at times after 1 ms) for the 0.98 m event, a lower value for the 1.2 m event, and the lowest value for the 0.686 m event. This difference is due in part to the lower coupling efficiency for the 0.686 m event, which tends to decrease kinetic energies coupled everywhere outside the rock-vapor region. The difference is also partly attributable to the mass of material in the vaporized-water region, which is greatest for the 0.98 m event and slightly less for the other two events (Fig. 6).

Finally, the kinetic and internal energies in solid rock are presented in Fig. 11. These energies have not been plotted separately for fractured and unfractured material, since rock failure is still occurring at 14 ms and the wave propagation will not become elastic until much later in the event history. The internal-energy curves cross at times earlier than 5 ms because of close-range coupling effects. However, after this time, the kinetic and internal energies in rock are always greatest for the 1.2 m event, less for the 0.98 m event, and least for the 0.686 m event. This outcome is completely consistent with the calculated displacements and reduced displacement potentials at very late times, which also show the most efficient overall coupling for the 1.2 m event and least-efficient coupling for the 0.686 m event. These energy results strongly support the proposed source-coupling explanation, i.e., the small-radius source generates very high pressure loading, vaporization, and waste-heat losses at close range. Thus, it couples less efficiently with the surrounding medium than a somewhat larger effective source of lower initial pressure.

It is of interest to closely examine kinetic-energy transfer to the rock for these three calculations. The maximum percentage of the total source energy transformed into kinetic energy is about 17%

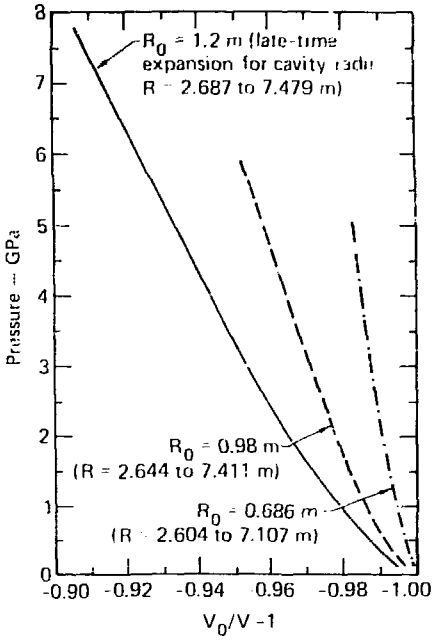

FIG. 8. Expansion of iron gas energy source region.

(1.2 m radius source), 15% (0.98 m radius source), or 14% (0.686 m radius source). The kinetic energy peaks at a relatively early time of about 2.5 to 3 ms, and declines steadily thereafter. These results may be compared with earlier studies of a very weak saturated mudstone, which showed about 17% kinetic energy transfer to the rock environment.[17] The cratering effectiveness of a near-surface detonation is closely related to kinetic energy coupling efficiency. Thus, the source-size effect revealed here indicates that the large-radius source might be the most efficient for cratering events, as well as for seismic energy coupling at greater depths.

STRESS WAVE ATTENUATION

The shape and attenuation of the outgoing stress wave are very sensitive to the initial energy density of the source in the region close to the source. Figure 12 shows the stress profile for three scaled source radii at a time of 10^{-4} s kt$^{1/3}$, which is just a few microseconds after vaporization of the rock has occurred. The location of the shock wave is essentially the same at this time, even though each wave has traveled considerably different distances from the initial source. The magnitudes of the peak stresses and their early time attenuation rates are considerably different.

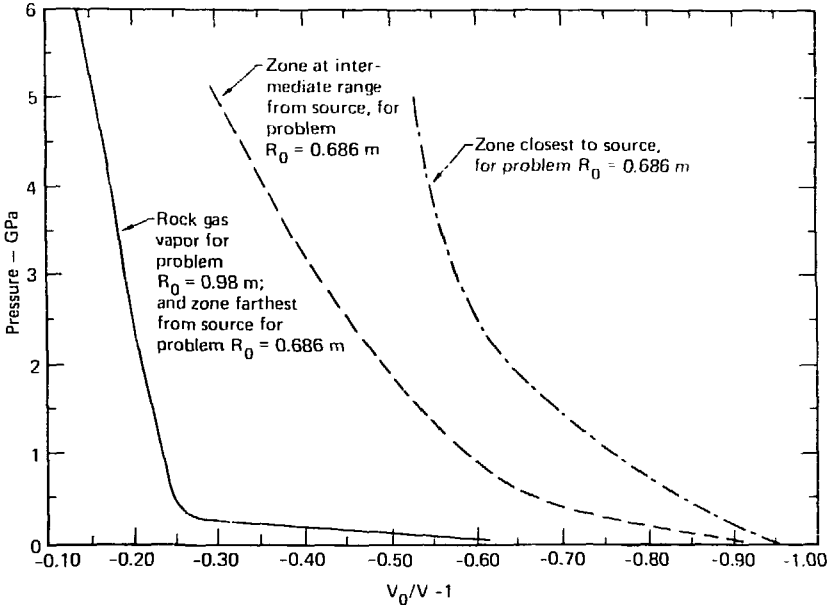

FIG. 9. Expansion of vaporized rock gas zone (average behavior); time = 0.5 to 15 ms.

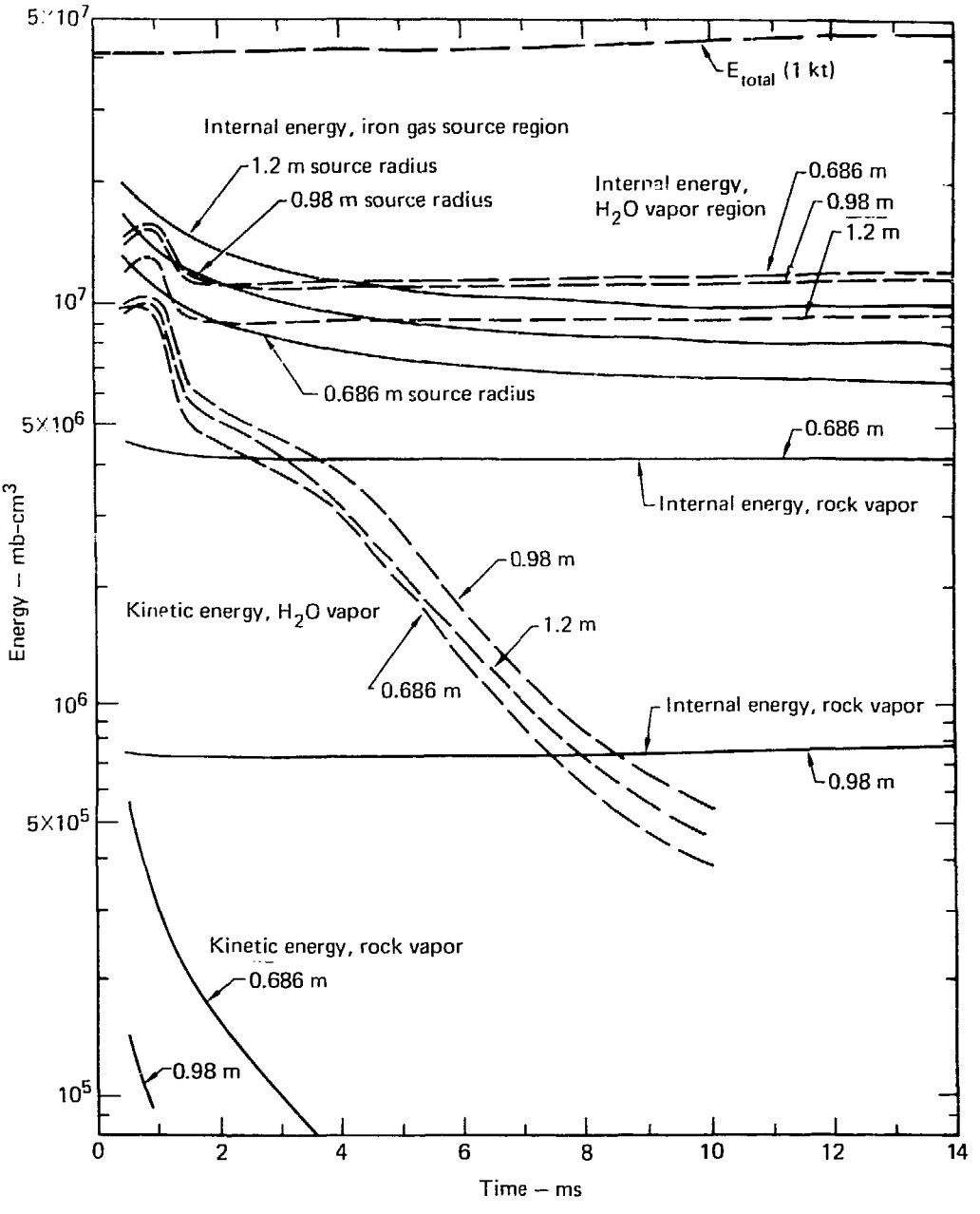

FIG. 10. Energy content of gas materials, 0.5 to 10 ms.

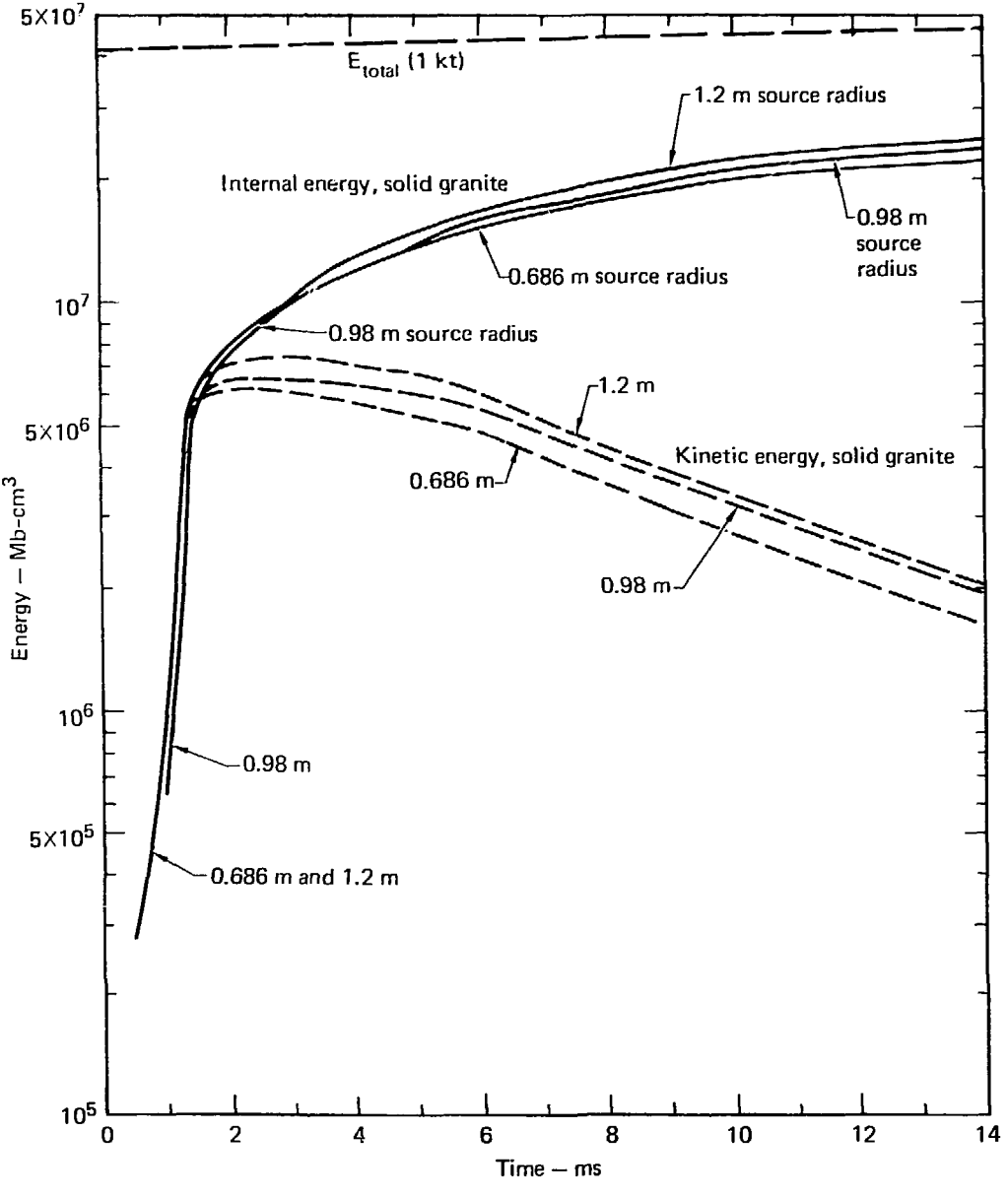

FIG. 11. Energy content in solid granite, 0.5 to 14 ms.

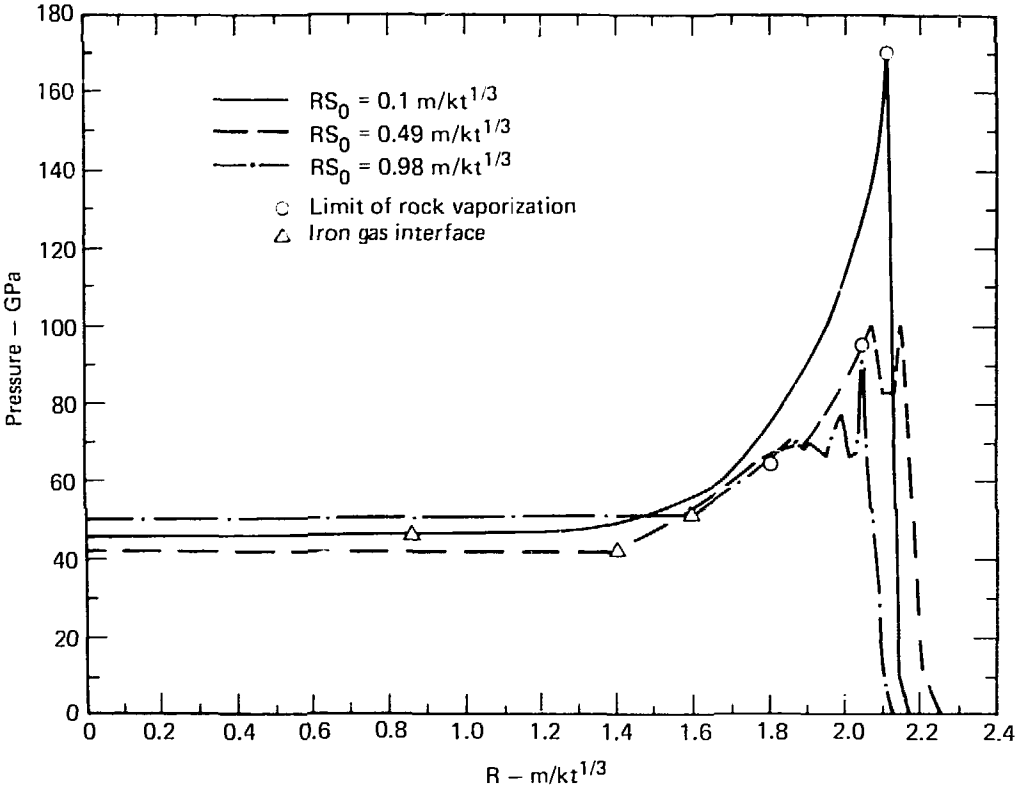

FIG. 12. Stress profile at $\bar{T} = 10^{-4}$ (s/kt$^{1/3}$).

The higher the initial energy density (the smaller the initial scaled source radii), the greater the stress magnitude and the greater the attenuation. The greater attenuation is a consequence of the larger amount of energy being deposited in the rock as was just discussed.

For those calculations that modeled a "tamped" detonation ($R_0 \leq 0.98$ m/kt$^{1/3}$), the magnitude and attenuation rate of the peak of the stress wave merged at about 4 m/kt$^{1/3}$ from the detonation center. Figure 13 shows the magnitude of the peak of the stress wave as a function of scaled distance. Four calculations are shown where the scaled source size varies from 0.1 to 3.0 m/kt$^{1/3}$. The peak stresses for scaled sources of less than or equal to 1.8 m/kt$^{1/3}$ merge at a distance of 20 m/kt$^{1/3}$. Thus over the range of scaled source radii where enhanced coupling is calculated, the magnitude of the stress wave at far distances from the source is independent of the scaled source size. This is in agreement with previous studies.[7] Only after an increase of the scaled source radii beyond 2.0 m/kt$^{1/3}$ does the peak of the stress wave begin to reflect the partial decoupling effects.

ELASTIC RESPONSE

An examination of some of the calculated earth-motion parameters in the elastic region yielded greater insight into the causes of enhanced seismic coupling effect. Figure 14 is a replot of the information shown in Fig. 4, with an enlarged linear scale so it can be compared with the following figures. Figures 15–19 show the peak stress, peak particle velocity, peak scaled displacement, scaled final displacement, and scaled reduced displacement potential in that order. These parameters were evaluated in the elastic region at a scaled distance

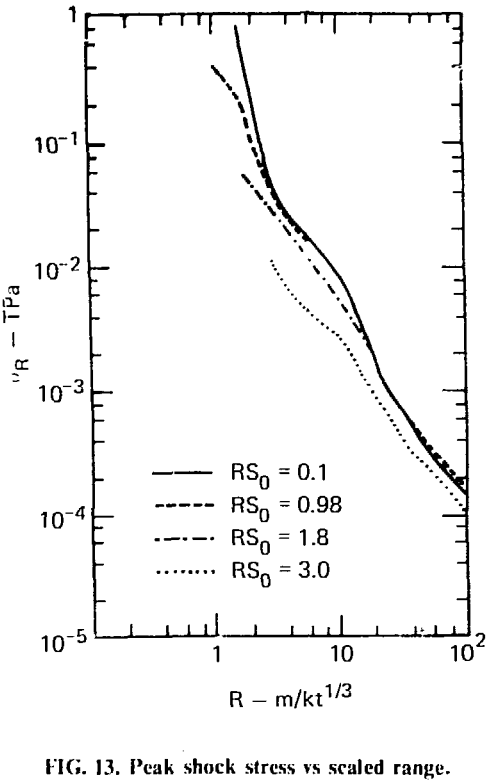

FIG. 13. Peak shock stress vs scaled range.

from the source of 100 m/kt$^{1/3}$ for each calculation with scaled source radii up to 4.0 m/kt$^{1/3}$. This covers the range of scaled source size over which enhanced seismic coupling was calculated.

Three observations can be made from Figs. 14–19:

1. There is some scatter in the calculated results because of small variations in zone size.

2. There is a definite discontinuity in all the parameters in the elastic region for scaled source size between 0.78 and 0.98 m/kt$^{1/3}$. This corresponds to the drastic change in the amount of rock vaporized as the scaled radius is varied over this source size interval.

3. All parameters in the elastic region decrease rapidly for scaled source radii greater than 2.0 m/kt$^{1/3}$.

The effect of the decrease in amount of rock vaporized appears to increase all variables shown in Figs. 15–19 by approximately 10%. There is also a noticeable effect on the radius of water vaporization and final cavity radii caused by the amount of rock vaporized, as can be seen in Fig. 14.

Figures 17 and 18 show the peak scaled displacement and final scaled displacement, respectively. The peak displacement is essentially the integration of the particle velocity over the first positive pulse and shows a substantially smaller increase with increased scaled source radii than does the final displacement. The peak particle velocity, being essentially constant over this interval of scaled source radii, suggests that the duration of the stress wave pulse is also sensitive to the scaled source size and plays an important role in the enhanced seismic coupling shown in Fig. 19.

Figure 20 is a plot of the scaled wavelength or time of duration of the main pulse and rebound pulse as the stress wave passes the point at a scaled distance of 100 m kt$^{1/3}$. This scale wavelength is plotted against the scaled source radii over the entire range of the parametric study. The scaled time duration of the first positive pulse λ_1 increases linearly with scaled source size up to values of 8.0 m kt$^{1/3}$. Between RS_0 = 8.0 m (kt)$^{1/3}$ and 10 m/kt$^{1/3}$ there is a sharp discontinuity in λ_1 which is probably because there is very little displacement at the cavity boundary for cavity source sizes greater than 8.0 m/kt$^{1/3}$ (see Fig. 4).

The first negative pulse length is essentially constant for a scaled source size, which varies from a point source to RS_0 = 2.0 m/kt$^{1/3}$, then decreases linearly to RS_0 = 10 m/kt$^{1/3}$ and remains essentially constant for scaled source sizes greater than 10 m/kt$^{1/3}$.

Since the displacement is roughly proportional to the product of particle velocity and the duration interval, the reason for the enhanced seismic coupling effect, apparent in Figs. 17–19, becomes clear by comparing Figs. 16 and 20. The increase of the scaled displacement or scaled reduced displacement potential with scaled source size less than 2.0 is due primarily to the product of a constant velocity and an increasing pulse duration interval. The decrease in the energy absorbed in vaporizing or melting the rock with increasing source size occurs over a very short range of scaled source size. The energy absorbed in vaporizing the rock is approximately 10% for $RS_0 \leq 0.8$, 2% for RS_0 = 1.0, and 0% for $RS_0 \geq 1.1$. The contribution to the enhanced seismic coupling effect caused by the decrease of energy absorbed in vaporization results in an approximately 7% increase in the peak particle

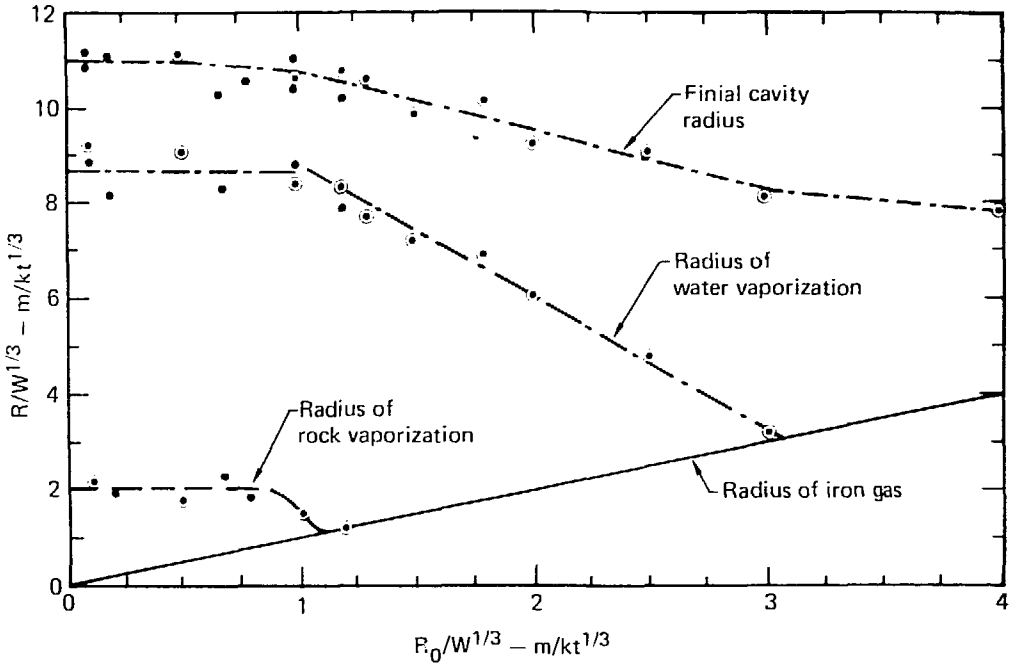

FIG. 14. Radii of major states of rock vs scaled initial source size.

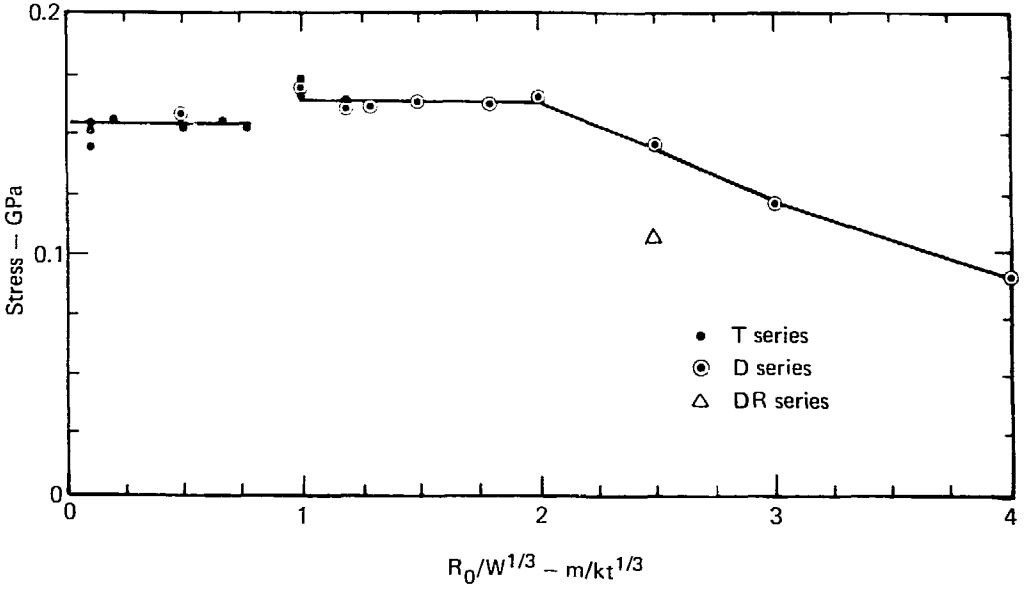

FIG. 15. Peak radial stress at scaled range of 100 $m/kt^{1/3}$ vs scaled source size.

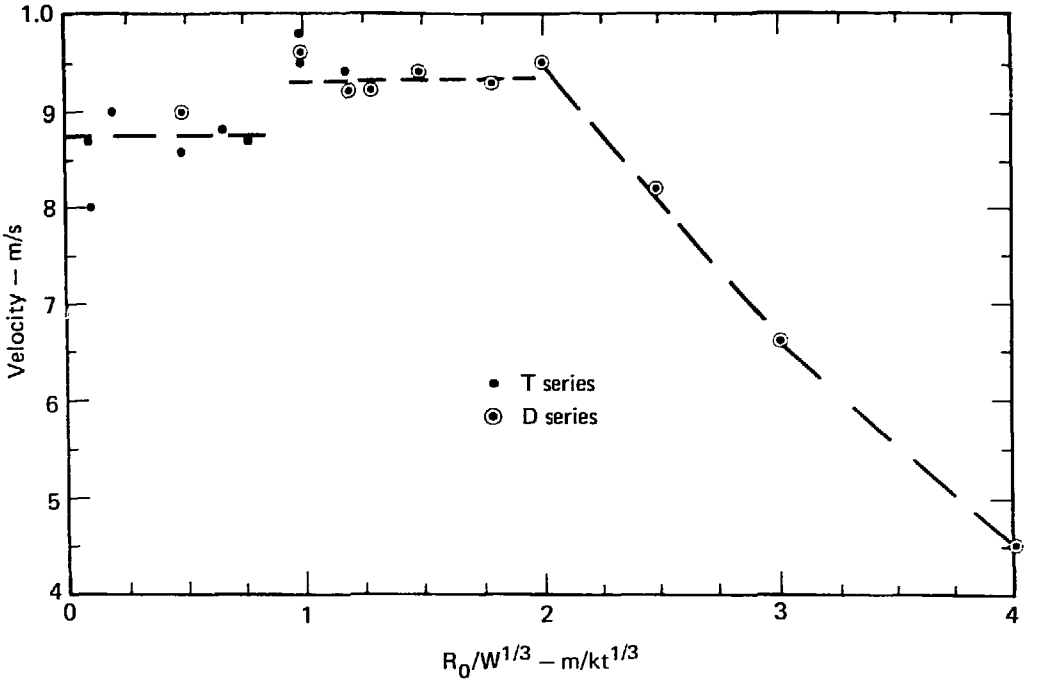

FIG. 16. Peak particle velocity at range of 100 m/kt$^{1/3}$ vs scaled source radius.

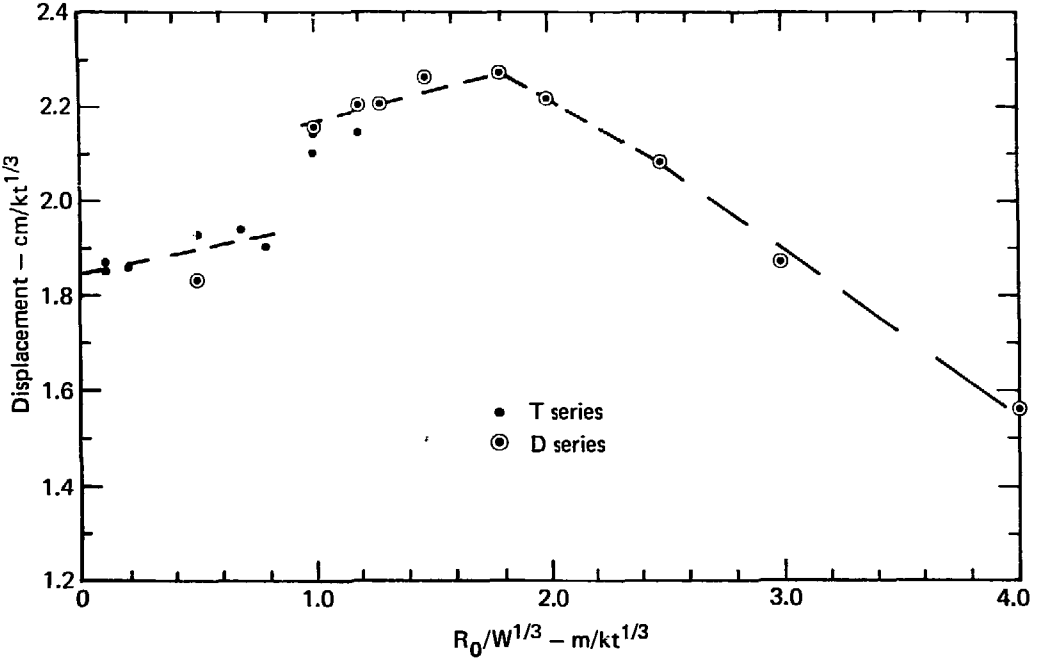

FIG. 17. Peak scaled displacement at scaled range of 100 m/kt$^{1/3}$ vs scaled source radius.

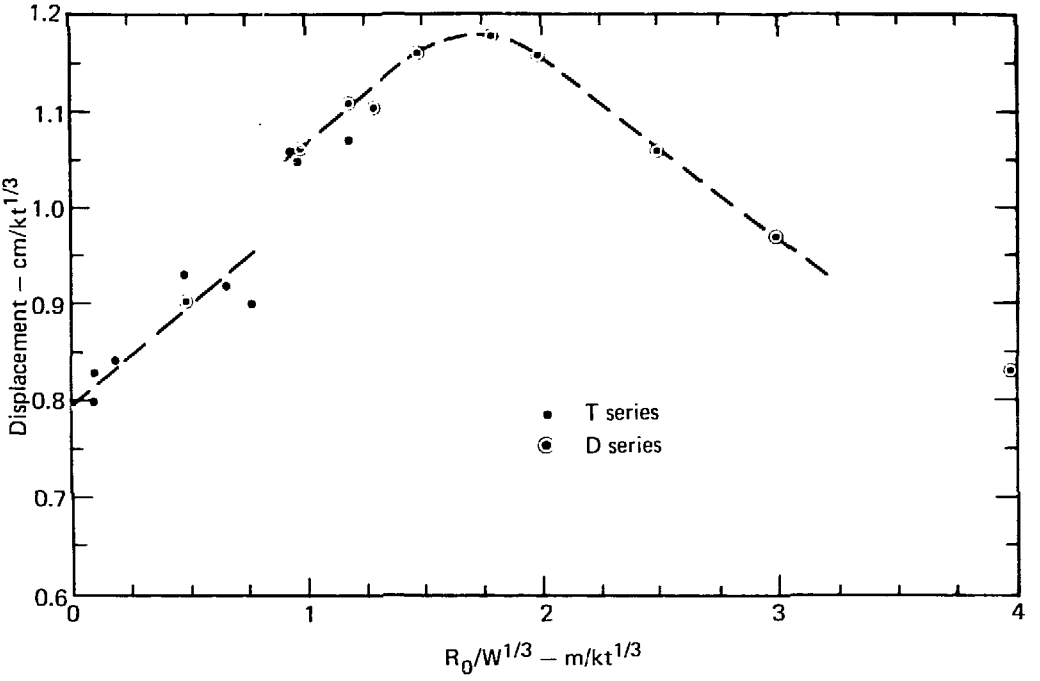

FIG. 18. Scaled final displacement at scaled range of 100 m/kt$^{1/3}$ vs scaled source radius.

velocity. The contribution of the increasing pulse duration interval to the enhanced seismic coupling effect is approximately 38% at maximum over a point source. Thus the major effect producing the enhanced seismic coupling in Fig. 19 is simply that larger sources produce longer wavelengths.

For scaled source radii greater than 2.0, there is a large decrease in the peak velocity with increasing source size. Since the particle velocity decrease is greater than the increase in wave pulse duration, there is a net decrease in the displacement for increasing source radii greater than 2.0. Thus the peak in the RDP (Figs. 2 and 19), occurring at approximately a scaled source size of 2.0 m/kt$^{1/3}$, is fully accounted for by the effect of the initial cavity size on the peak particle velocity and pulse duration. The net energy available by not vaporizing the rock is only a secondary and relatively minor contribution to the enhanced RDP. Based on the simple approximation inherent in this parameter study, it appears that a detonation in a cavity with a radius of 15 m/kt$^{1/3}$ is essentially decoupled and little is gained in going to larger cavities.

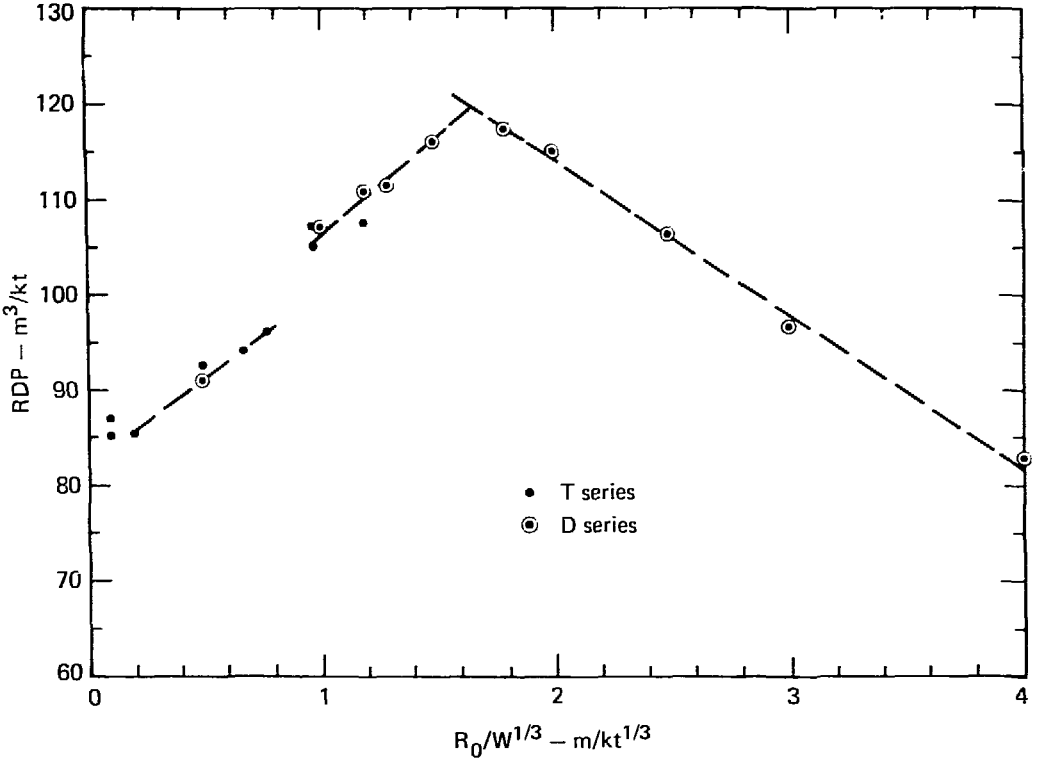

FIG. 19. Scaled reduced displacement potential vs scaled source radius.

DISCUSSION WITH RESPECT TO SOME NTS NUCLEAR EVENTS

Table 3 presents scaled emplacement data for 12 recent nuclear tests in the Pahute Mesa, Yucca Flat, and Rainier Mesa areas at the Nevada Test Site (NTS). The scaled mass (kg/kt) for the Pahute Mesa and Yucca Flat explosions is based on the total mass of the canister containing the explosive. For the explosions in Rainier Mesa, the scaled mass is based on the mass of the steel walls of the shot room plus the contents of the room. The scaled radius ($m/kt^{1/3}$) for the explosions is that for a sphere of volume equal to that of the canister (explosions 1, 2, 5–8) or shot room (explosions 3, 4, 9–12). The canisters for explosions 3 and 4 in Pahute Mesa and for explosion 9 in Yucca Flat were emplaced in larger, air-filled cavities that had been mined at the bottom of the emplacement holes. The

TABLE 3. Explosion emplacement data.

Area	Event No.	R_0 ($m/kt^{1/3}$)	M (kg/kt)
Pahute Mesa	1	0.10	13.0
	2	0.11	4.7
	3	0.29	3.0
	4	0.34	2.3
Yucca Flat	5	0.36	171
	6	0.54	660
	7	0.55	520
	8	0.47	615
	9	0.86	18.4
Rainier Mesa	10	0.83	365
	11	1.12	780
	12	1.23	755

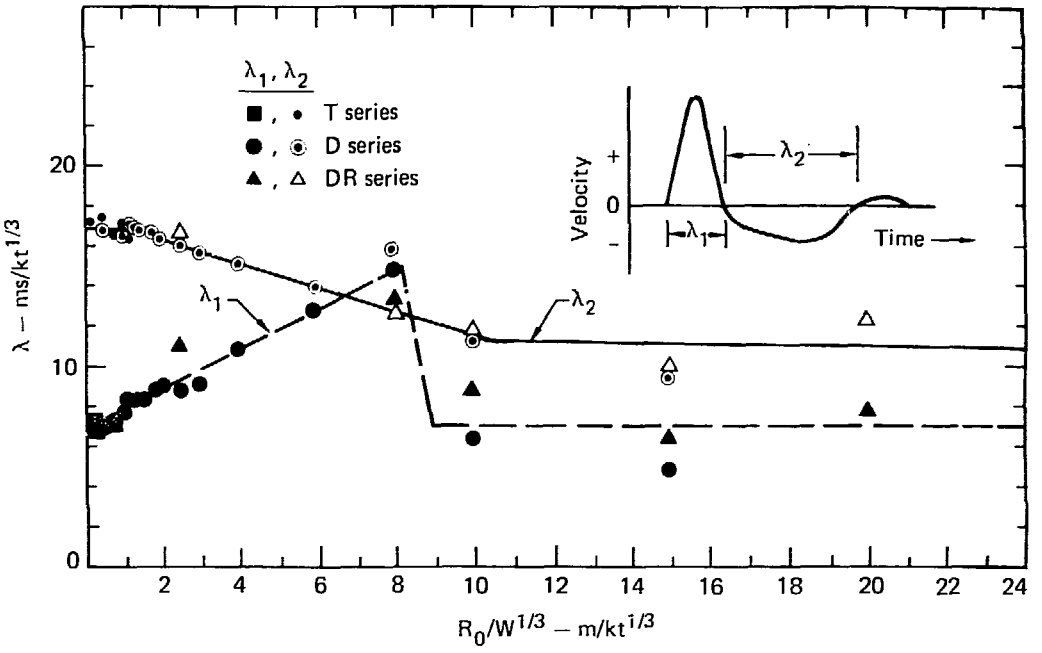

FIG. 20. Scaled wavelength vs scaled source radius.

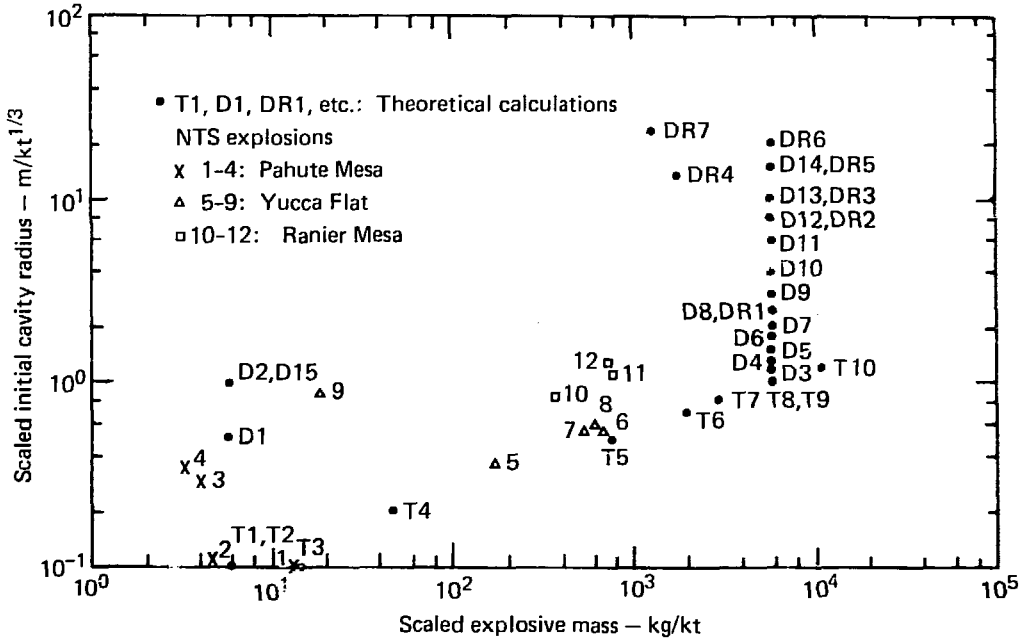

FIG. 21. Comparison of scaled explosive mass vs scaled initial cavity radius for theoretical calculations and NTS explosions.

space between the canister and the walls of the emplacement holes for the other explosions in Pahute Mesa and Yucca Flat was filled with stemming material (e.g., sand or pea gravel). The space between the shot-room walls and the surrounding rock in Rainier Mesa was filled with grout.

The scaled radii and scaled masses for both the NTS explosions and the calculations are plotted in Fig. 21. The NTS events fall within the same range assumed for the tamped calculations (0.1 to 1.3 $m/kt^{1/3}$). It is also shown that the scaled radii vs scaled mass relations for two of the Pahute Mesa explosions (events 1 and 2) and most Yucca Flat explosions (events 5–8) approximate those for the constant mass that was assumed for most of the tamped calculations. The scaled mass for the two Pahute Mesa explosions (events 3 and 4), one Yucca Flat explosion (event 9), and all the Rainier Mesa explosions (events 10–12), which were in mined cavities or shot rooms is less, for a given scaled radius, than that for the hypothetical explosions. We have shown in the preceding sections that, for the ranges of conditions considered, scaled radius has significantly more effect than scaled mass on seismic coupling.

Figure 19 shows the final value of scaled reduced displacement potential (RDP) as a function of the scaled energy source radius for the tamped calculations. If the calculational results are applicable to the explosions listed in Table 3, we would expect the emplacement conditions to produce the weakest relative seismic coupling for Pahute Mesa explosions (small scaled source radii), and the strongest coupling for explosions in Rainier Mesa (near-optimum scaled source radii).

The seismic magnitude (m_b) data[18] for NTS explosions indicate that the seismic signals (normalized to a common yield, assuming a common slope for the m_b vs $\log_{10}$ yield relations) from Rainier Mesa explosions are, on the average, a fraction of a magnitude unit greater than those from explosions below the water table in Yucca Flat and Pahute Mesa. This result is consistent with the scaled source radius vs scaled RDP results shown in the figure. However, the qualitative agreement of these results does not prove that the differences in scaled radius alone are responsible for the somewhat stronger signals from Rainier Mesa explosions. Other emplacement and geological factors (depth, shot-point rock properties, local geological structure) that affect signal generation and propagation could be responsible for all or part of the observed seismic magnitude difference.

Two of the Pahute Mesa explosions (1 and 2) have a scaled radius of about 0.1 $m/kt^{1/3}$ and the other two (3 and 4) have a scaled radius of about 0.3 $m/kt^{1/3}$. The results of our calculations shown in Figs. 2 and 19 indicate that the seismic coupling of the latter explosions should be somewhat stronger. However, the magnitude residuals from the magnitude vs $\log_{10}$ yield relation for Pahute Mesa, when plotted as a function of scaled radius, show no such trend for these four explosions. The scatter of the magnitude residuals for Pahute Mesa is probably determined by other variations in seismic signal generation and transmission, not by variations in scaled radius.

Similarly, the coupling of explosions 5 and 9 in Yucca Flat might be different because of the difference in scaled radius. However, the observed coupling for these two explosions is almost exactly equal to the mean coupling observed below the water table in Yucca Flat.

We conclude that the above field data do not provide sufficient evidence to either support or negate the enhanced coupling that is indicated by our calculations for scaled cavity radii of 1 to 2 $m/kt^{1/3}$.

ACKNOWLEDGMENTS

We appreciate the assistance of the following people in providing emplacement data for NTS nuclear explosions: C. E. Walter, D. E. Walton, and W. Wakeman of the Lawrence Livermore Laboratory, J. W. LaComb of Defense Nuclear Agency Field Command, and C. R. Dismukes of Systems, Science and Software.

J. G. Trulio of Applied Theory, Incorporated, suggested this area of research and performed the first calculations demonstrating the enhanced coupling effect. He has provided useful information and comments during the course of this project.

The work discussed in this report was sponsored by the Advanced Research Projects Agency and performed under the auspices of the U.S. Department of Energy.

REFERENCES

1. D. W. Patterson, "Nuclear Coupling, Full and Partial," *J. Geophys. Res.* **71**, 3427 (1966).
2. D. W. Patterson, *The Calculational Sensitivity of a Model Describing the Reponse of a Nuclear Formed Cavity*, Lawrence Livermore Laboratory, Livermore, CA, Rept. UCID-5125 (1966).
3. F. G. P. Seidl, *SOC, A Numerical Model for Behavior of Materials Exposed to Intense Impulsive Stresses*, Lawrence Livermore Laboratory, Livermore, CA, Rept. UCID-5033 (1965).
4. J. T. Cherry and F. L. Petersen, "Numerical Simulation of Stress Wave Propagation from Underground Nuclear Explosions," in *Symp. on Engineering with Nuclear Explosives* (ANS-CONF 700101, Las Vegas, NV, January 1970), Vol. 1.
5. J. F. Schatz, *SOC73, A One-Dimensional Wave Propagation Code for Rock Media*, Lawrence Livermore Laboratory, Livermore, CA, Rept. UCRL-51689 (1974).
6. C. M. Snell, *User's Manual for SOC74*, Lawrence Livermore Laboratory, Livermore, CA, Rept. RKCD 76-12 (1976).
7. R. C. Schroeder, *A Comparison of Initial Conditions for Nuclear Explosion Calculations*, Lawrence Livermore Laboratory, Livermore, CA, Rept. UCRL-51671 (1974).
8. W. E. Baker, P. S. Westine, and F. T. Dodge, *Similarity Methods in Engineering Dynamics* (Spartan Books, Hayden Book Co., Rochelle Park, NJ, 1973).
9. S.L. Hancock, *Numerical Convergence to Mechanical Equilibrium with a Velocity Damping Method and its Interpretation as Simultaneous Over-relaxation*, Physics International Company, San Leandro, CA, Rept. TCAM 73-8 (1973).
10. T. R. Butkovich, *The Gas Equation of State for Natural Materials*, Lawrence Livermore Laboratory, Livermore, CA, Rept. UCRL-14729 (1967).
11. T. R. Butkovich, "Calculation of the Shock Wave from an Underground Nuclear Explosion in Granite," *J. Geophys. Res.* **70**, 885 (1965).
12. J. T. Cherry and E. G. Rapp, *Calculation of Free-field Motion for the Piledriver Event*, Lawrence Livermore Laboratory, Livermore, CA, Rept. UCRL-50373 (1968).
13. J. T. Cherry and F. L. Petersen, "Numerical Simulation of Stress Wave Propagation from Underground Nuclear Explosions," in *Engineering with Nuclear Explosives*, CONF-700101 (American Nuclear Society, Las Vegas, NV 1970), Vol. 1.
14. J. F. Schatz, Lawrence Livermore Laboratory, Livermore, CA, private communication.
15. T. R. Butkovich, Lawrence Livermore Laboratory, Livermore, CA, private communication.
16. R. W. Terhune, *Analysis of Depth of Burial Criteria for Containment*, Lawrence Livermore Laboratory, Livermore, CA, Rept. UCRL-52395 (1978).
17. D. E. Burton, C. M. Snell, and J. B. Bryan, "Computer Design of High-Explosive Experiments to Simulate Subsurface Nuclear Detonations," *Nucl. Tech.* **26**, 65 (1975).
18. R. W. Alewine III, AFTAC/VSC, private communication.

REH/bg

APPENDIX A
INITIAL CONDITIONS

Abbreviations used in Tables A-1 - A-3

W Yield, kt
R_0 Initial cavity radius, m
RM Radius of grid boundary, m
NC Number of zones in source cavity
NT Number of zones in calculation
ZA Initial zone size at cavity boundary, m
ZL Zone size at range of 100 m, m
M_0 Mass of iron for source, Mg
ρ_0 Initial density of source, Mg/m^3
P_0 Initial pressure of source
E_0 Initial energy density
RS_0 Scaled source radius, $m/kt^{1/3}$
ZAS Scaled zone size ZA, $m/kt^{1/3}$
ZLS Scaled zone size ZL, $m/kt^{1/3}$

TABLE A-1. Initial conditions for tamped (T) calculations.

	Parameters													
	W (kt)	R_0 (m)	RM (m)	NC	NT	ZA (m)	ZL (m)	M_0 (Mg)	ρ_0 (Mg/m^3)	E_0 (TPa)	P_0 (TPa)	ZAS ($m/kt^{1/3}$)	ZLS ($m/kt^{1/3}$)	RS_0 ($m/kt^{1/3}$)
T1	1000	0.98	3000	10	1000	0.10	5.2	5.91	1.5	1.1+3	4.2+2	0.01	0.52	0.1
T2	1000	0.98	3000	25	1015	0.035	6.4	5.91	1.5	1.1+3	4.2+2	0.0035	0.64	0.1
T3	1.0	0.1	600	10	710	0.011	0.89	0.014	3.23	1.1+3	4.4+2	0.011	0.89	0.1
T4	125	0.98	1500	10	1000	0.10	2.2	5.91	1.5	1.5+2	5.6+1	0.02	0.44	0.2
T5	8.0	0.98	850	25	805	0.04	1.4	5.91	1.5	8.5	3.0	0.02	0.07	0.5
T6	1.0	0.686	600	7	788	0.10	0.52	2.03	1.5	3.1	1.1	0.10	0.52	0.7
T7	2.0	0.98	600	10	1000	0.10	0.40	5.91	1.5	2.1	0.74	0.08	0.32	0.8
T8	1.0	0.98	600	25	1015	0.04	0.45	5.91	1.5	1.1	0.38	0.04	0.45	1.0
T9	1.0	0.98	600	10	1090	0.10	0.33	5.9	1.5	1.1	0.38	0.10	0.33	1.0
T10	1.0	1.2	600	12	793	0.10	0.51	10.9	1.5	0.58	0.21	0.10	0.51	1.2

TABLE A-2. Initial conditions for decoupled (D) calculations.

	Parameters													
	W (kt)	R_0 (m)	RM (m)	NC	NT	ZA (m)	ZL (m)	M_0 (Mg)	ρ_0 (Mg/m^3)	E_0 (TPa)	P_0 (TPa)	ZAS (m/kt$^{1/3}$)	ZLS (m/kt$^{1/3}$)	RS_0 (m/kt$^{1/3}$)
D1	1000	4.9	3000	10	780	0.5	5.0	5.91	1.2-2	8.5	2.9	0.05	0.5	0.5
D2	1000	9.8	3000	10	780	1.0	4.0	5.9	1.5-3	1.1	0.35	0.1	0.4	1.0
D3	1.0	1.2	600	30	830	0.04	0.71	5.9	0.82	0.58	0.19	0.04	0.71	1.2
D4	1.0	1.3	600	13	813	0.09	0.59	5.9	0.64	0.46	0.15	0.09	0.59	1.3
D5	1.0	1.5	600	15	715	0.09	0.59	5.9	0.42	0.30	9.5-2	0.09	0.59	1.5
D6	1.0	1.8	600	18	718	0.09	0.59	5.9	0.24	0.17	5.4-2	0.09	0.59	1.8
D7	1.0	2.0	600	15	1015	0.12	0.38	5.9	0.18	0.13	3.8-2	0.12	0.38	2.0
D8	1.0	2.5	600	25	725	0.09	0.58	5.9	9.0-2	6.4-2	1.9-2	0.09	0.58	0.25
D9	1.0	3.0	600	12	712	0.22	0.54	5.9	5.2-2	3.7-2	1.1-2	0.22	0.54	3.0
D10	1.0	4.0	600	15	715	0.24	0.60	5.9	2.2-2	1.6-2	4.3-2	0.24	0.60	4.0
D11	1.0	6.0	600	15	715	0.25	0.53	5.9	6.5-2	4.63	1.2	0.25	0.60	6.0
D12	1.0	8.0	600	22	658	0.10	0.62	5.9	2.8-3	1.95	0.45	0.10	0.53	8.0
D13	1.0	10	600	100	700	0.10	0.62	5.9	1.4-3	1.0	0.22	0.10	0.62	10
D14	1.0	15	600	136	736	0.10	0.61	5.9	4.2-4	0.3	6.0-2	0.10	0.61	15

TABLE A-3. Initial conditions for decoupled relaxation (DR) calculations.

	Parameters													
	W (kt)	R_0 (m)	RM (m)	NC	NT	ZA (m)	ZL (m)	M_0 (Mg)	ρ_0 (Mg/m^3)	E_0 (GPa)	P_0 (GPa)	ZAS (m/kt$^{1/3}$)	ZLS (m/kt$^{1/3}$)	RS_0 (m/kt$^{1/3}$)
DR1	1.0	2.5	450	5	309	1.47	1.47	5.91	9.0-2	6.4	19.0	1.47	1.47	2.5
DR2	1.0	8.0	450	10	310	1.47	1.47	5.91	2.8-3	1.95	0.45	1.47	1.47	8.0
DR3	1.0	10.0	450	12	305	1.50	1.50	5.91	1.4-3	1.0	0.22	1.50	1.50	10
DR4	1.0	15.0	450	15	305	1.50	1.50	5.91	4.2-4	0.296	0.060	1.50	1.50	15
DR5	1.0	20.0	450	20	307	1.50	1.50	5.91	1.8-4	0.125	0.025	1.50	1.50	20
DR6[a]	1.0	13.81	450	15	306	1.50	1.50	1.82	1.6-4	0.38	0.07	1.50	1.50	13.81
DR7[a]	1.0	23.62	450	25	309	1.50	1.50	1.36	2.5-5	0.076	0.013	1.50	1.50	23.62

[a]Initial overburden stress of 18 MPa.

APPENDIX B
SCALED RESULTS

Abbreviations used in Tables B-1–B-3

W	Yield, kt
RS_0	Source size, $m/kt^{1/3}$
RRV	Radius of rock vaporization, $m/kt^{1/3}$
RWV	Radius of water vaporization, m/kt
RFL	Radius of rock fracture limit on loading, $m/kt^{1/3}$
RFU	Radius of maximum rock fracture, $m/kt^{1/3}$
RC	Final cavity radius, $m/kt^{1/3}$
PC	Final cavity pressure, MPa
ECR	Ratio of final cavity energy to yield
ERR	Ratio of energy in fracture rock to yield
ESR	Ratio of seismic energy to yield
RDP	Scaled reduced displacement potential, m^3/kt
λ_1	Scaled positive pulse duration, $ms/kt^{1/3}$
$\lambda_2 + \lambda$	Scaled total pulse duration, $ms/kt^{1/3}$

TABLE B-1. Scaled results for tamped (T) calculations.

	Parameters													
	W (kt)	RS_0 ($m/kt^{1/3}$)	RRV ($m/kt^{1/3}$)	RWV (m/kt)	RFL ($m/kt^{1/3}$)	RFV ($m/kt^{1/3}$)	RC ($m/kt^{1/3}$)	PC (MPa)	ECR	ERR	ESR	RDP (m^3/kt)	λ_1	$\lambda_2+\lambda_1$
T1	1000	0.1	2.03	9.5	51.6	77.8	11.2	48.5	0.534	0.419	6.0-2	85.0	6.8	23.6
T2	1000	0.1	2.12	9.2	51.4	78.0	11.0	59.0	0.520	0.424	6.2-2	87.0	–	–
T3	1.0	0.1	2.23	8.86	51.1	77.2	10.9	48.9	0.533	0.420	5.7-2	85.0	7.2	24.0
T4	125	0.2	2.01	8.16	52.0	77.8	11.1	48.7	0.537	0.415	6.1-2	85.2	–	–
T5	8.0	0.5	1.93	9.0	52.5	79.4	11.0	61.4	0.510	0.449	6.2-2	92.5	–	–
T6	1.0	0.7	2.31	8.28	53.0	79.5	10.3	73.8	0.495	0.456	6.4-2	94.0	–	–
T7	2.0	0.8	1.90	8.50	53.7	80.2	10.6	74.2	0.481	0.458	6.7-2	96.0	–	–
T8	1.0	1.0	1.62	8.8	53.9	82.7	11.0	75.9	0.443	0.489	7.3-2	105	–	–
T9	1.0	1.0	1.68	8.4	55.0	82.0	10.4	75.0	0.426	0.504	7.7-2	107	–	–
T10	1.0	1.2	–	7.9	53.7	83.2	10.2	87.3	0.416	0.514	7.2-2	107.5	–	–

TABLE B-2. Scaled results for decoupled (D) calculations.

	Parameters													
	W (kt)	RS_0 ($m/kt^{1/3}$)	RRV ($m/kt^{1/3}$)	RWV (m/kt)	RFL ($m/kt^{1/3}$)	RFV ($m/kt^{1/3}$)	RC ($m/kt^{1/3}$)	PC (MPa)	ECR	ERR	ESR	RDP (m^3/kt)	λ_1	$\lambda_2+\lambda_1$
D1	1000	0.5	1.96	9.11	54.0	79.2	11.10	59.5	0.507	0.437	6.4-2	91.0	7.0	23.8
D2	1000	1.0	1.6	8.4	54.0	83.4	10.5	73.6	0.418	0.506	7.9-2	107.0	7.8	24.4
D3	1.0	1.2	–	8.3	53.5	84.3	10.8	83.3	0.402	0.525	7.4-2	111.0	8.2	25.2
D4	1.0	1.3	–	7.7	55.0	83.8	10.6	89.6	0.392	0.535	7.2-2	111.5	8.4	25.2
D5	1.0	1.5	–	7.2	54.0	82.0	9.9	97.0	0.374	0.554	7.5-2	116.0	8.4	25.0
D6	1.0	1.8	–	6.9	53.0	84.7	10.2	113	0.353	0.573	7.5-2	117.5	8.8	25.4
D7	1.0	2.0	–	6.12	53.0	82.0	9.3	125	0.357	0.569	7.5-2	115.0	9.0	25.2
D8	1.0	2.5	–	4.78	51.0	81.9	9.1	168	0.396	0.541	6.3-2	106.5	8.8	24.8
D9	1.0	3.0	–	3.22	42.0	78.5	8.1	215	0.463	0.490	4.9-2	97.0	9.2	24.8
D10	1.0	4.0	–	–	39.0	72.5	7.85	300	0.597	0.375	3.0-2	83.0	10.8	25.8
D11	1.0	6.0	–	–	20	57.0	7.7	420	0.831	0.159	1.1-2	49.5	–	–
D12	1.0	8.0	–	–	18	40.6	8.6	362	0.962	3.5-2	3.6-3	19.4	–	–
D13	1.0	10.0	–	–	13.6	27.9	10.2	210	0.994	4.6-3	1.2-3	6.2	–	–
D14	1.0	15	–	–	–	16.4	15.1	60.3	0.9998	1.8-5	2.1-4	1.2	–	–

TABLE B-3. Scaled results for decoupled relaxed (DR) calculations.

	Parameters													
	W (kt)	RS_0 ($m/kt^{1/3}$)	RRV ($m/kt^{1/3}$)	RWV (m/kt)	RFL ($m/kt^{1/3}$)	RFV ($m/kt^{1/3}$)	RC ($m/kt^{1/3}$)	PC (MPa)	ECR	ERR	ESR	RDP (m^3/kt)	λ_1	$\lambda_2+\lambda_1$
DR1	1.0	2.5	–	5.44	51	83.5	9.7	157	0.405	0.569	4.8-2	111.0	11.0	27.6
DR2	1.0	8.0	–	–	18	43.4	9.8	355	0.959	4.0-2	3.4-2	21.2	12.8	26.0
DR3	1.0	10	–	–	19.0	31.0	11.6	208	0.993	6.2-3	1.3-3	7.5	8.8	20.4
DR4	1.0	15	–	–	–	19.5	16.5	60.2	0.9995	5.3-5	8.9-5	2.4	6.4	16.2
DR5	1.0	20	–	–	–	23.0	21.5	24.7	1.0	–	–	2.07	7.8	20.2
DR6[a]	1.0	13.81	–	–	–	24.3	15.3	69.0	0.9993	3.1-4	2.7-4	2.7	6.8	17.2
DR7[a]	1.0	23.62	–	–	–	–	25.1	13.1	1.0	–	–	1.8	8.4	23.0

[a]Initial overburden stress of 18 MPa.